LUND UNIVERSITY
Faculty of Science

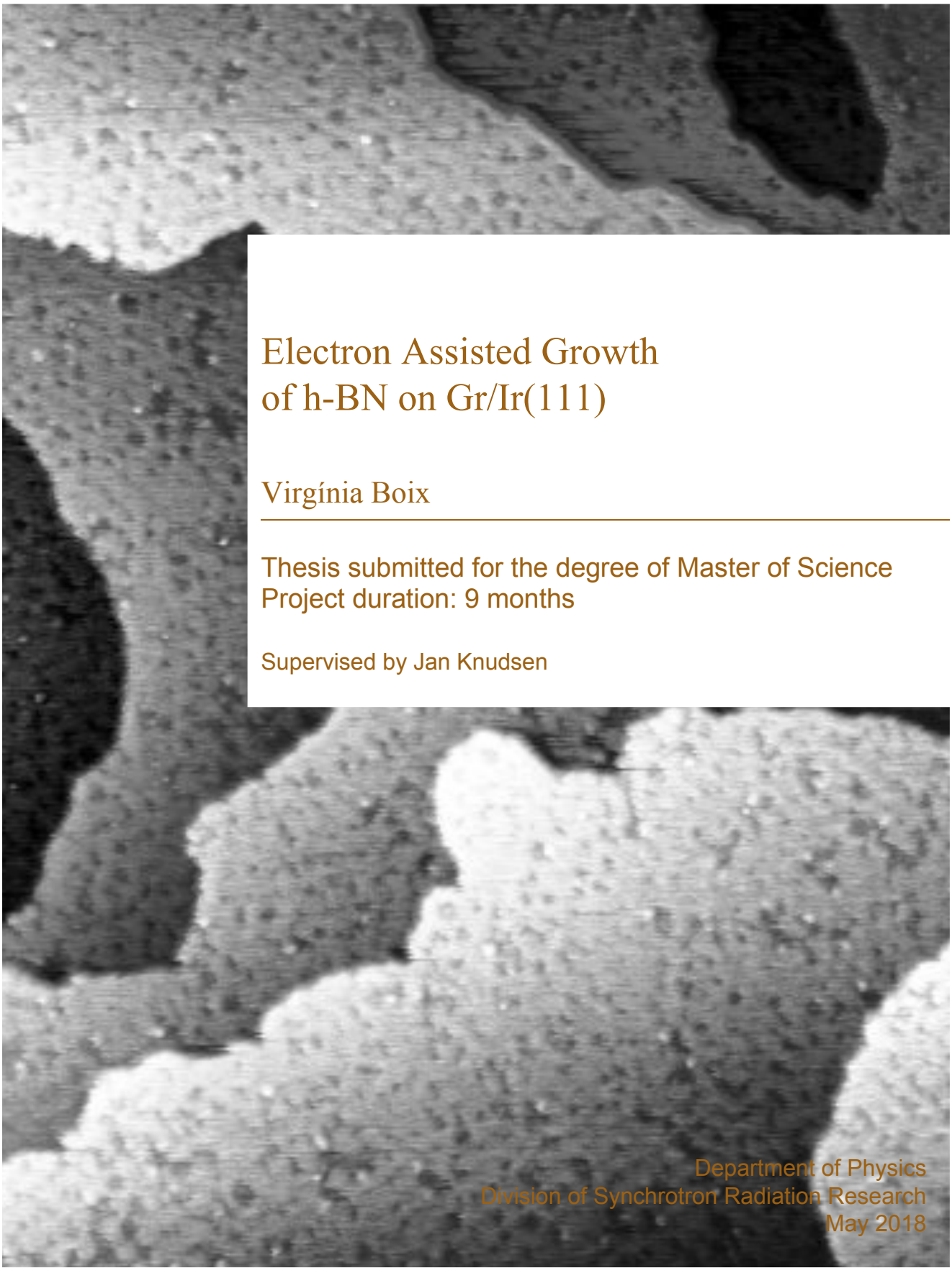

Electron Assisted Growth of h-BN on Gr/Ir(111)

Virgínia Boix

Thesis submitted for the degree of Master of Science
Project duration: 9 months

Supervised by Jan Knudsen

Department of Physics
Division of Synchrotron Radiation Research
May 2018

Master Thesis Project May, 2018

Electron Assisted Growth of h-BN on Gr/Ir(111)

Virgínia Boix

Project supervised by Jan Knudsen

Department of Physics, Division of Synchrotron Radiation Research

Abstract

Stacked heterostructures of two-dimensional (2D) materials are emerging as promising building blocks for a wide range of applications. These devices, which range from tunneling transistors to light-emitting diodes, use the properties of 2D materials that are not accessible by their bulk counterparts. However, with the current growth techniques, a scalable mass production of high-quality 2D heterostructures in any substrate cannot be achieved.

Here we present a novel method for direct growth of 2D materials on inert substrates; *Electron Assisted Growth*. It is based on an electron beam generated by a hot filament placed near the surface. The electrons dissociate the precursor molecules that become highly reactive radicals and adsorb on the substrate, where they form a crystalline structure upon annealing. The method has been employed to successfully grow a boron nitride (BN) layer atop one monolayer of graphene (Gr). XPS and STM characterization have shown additional traits of the BN formation, such as the low-temperature crystallization of the BN layer atop Gr or the role of the Gr layer as a filter for atomic species that diffuse underneath.

The results obtained show *Electron Assisted Growth* as a powerful and simple tool for growing 2D materials. Its easy implementation and scalability to other 2D materials and other substrates pave the way to direct fabrication of 2D heterostructure-based devices.

Acknowledgements

First of all, I would like to thank my supervisor, Jan Knudsen. Thank you for teaching me everything I need to know to survive in the lab, for your patience while solving all my questions and for the trust, you deposited in me. Your energy and motivation are really contagious! I would also like to thank Foteini for introducing me to this field! Tamires, for all the shared hours in the beamline and the improvised fikas. It wouldn't have been the same without you. Niclas, thanks for keeping the motivation up during the night shifts in Arhus, and for the improvised (and priceless) Igor lessons!

I would also like to thank the "STM crew", especially Estephania and Stephano, thanks for all the support and guidance with our lovely Obelix. Nikolay, thanks for helping me during my first time alone in an STM lab, I learned a lot with you. Thanks to the HIPPIE team at MaxIV for all the guidance and support during my first time in a beamline, even though you enjoyed a bit too much scaring me opening valves unexpectedly ;)

A big thanks go to my family and friends for all the support. To my peers, Kotte, Silvia, Anna, Axel, Henny,... your support (and the occasional rydberg's nights) helped me recover my confidence in desperate times. To my girls, Ebba, Julian, Christina, Hanna, thanks for always being there :) And to my family, for believing in me and for all the help with the design of the thesis. And finally, Jack. Thanks for letting me ramble on about my experiments (a bit too much :)) and for picking me up every time I doubted myself, you always brighten my day.

Contents

List of Abbreviations **vi**

1 Introduction **1**

2 Experimental techniques **4**
2.1 Scanning Tunneling Microscopy 4
2.2 X-Ray Photoemission Spectroscopy 7
2.2.1 Core-level binding energies 7
2.2.2 Features and lineshapes in XPS 9
2.2.3 The light source 10
2.2.4 The beamline 12

3 Results and discussion **13**
3.1 Growth of 2D materials on iridium substrate 13
3.1.1 The substrate: Ir(111) 13
3.1.2 Graphene growth on Ir(111) 14
3.1.3 Hexagonal boron Nitride on Ir(111) 16
3.2 Electron assisted growth of h-BN on Gr 19
3.2.1 Step 1: Borazine dosing with the molecule cracker 19
3.2.2 Step 2: Temperature evolution 28

4 Conclusions **37**

5 Outlook **39**

Appendices **44**

A Parameters for XPS fitting **44**

B Additional STM images **50**

List of Abbreviations

Gr ..... Graphene

BN ..... Boron Nitride

h-BN ..... hexagonal-Boron Nitride

CVD ..... Chemical Vapor Deposition

TPG ..... Temperature Assisted Growth

UHV ..... Ultra High Vacuum

RT ..... Room Temperature

ML ..... Monolayer

XPS ..... X-Ray Photoemission Spectroscopy

STM ..... Scanning Tunneling Microscopy

LEED ..... Low-Energy Electron Diffraction

LEEM ..... Low-Energy Electron Microscopy

LEER ..... Low-Energy Electron Reflectivity

GFWHM .. Gaussian Full Width Half Maximum

LFWHM .. Lorenzian Full Width Half Maximum

1 Introduction

Two-dimensional materials are crystalline solids consisting of a single layer of atoms. All of them present a strong in-plane bonding, which actively confines the charge and the phonon transport within each layer. This confinement gives 2D materials some unusual physical properties, such as high electron mobility or high thermal conductivity, which are not observed in their bulk counterparts. The unique properties make two-dimensional materials promising candidates for a wide range of applications, including the next generation of high-performance electronic devices. In addition, the rich physics exhibited by 2D materials also stimulated extensive research efforts in the fundamental physics of such layers in the past decade [1].

One of the most studied 2D materials is graphene, a single-atomic crystalline film of carbon isolated for the first time in 2004 by Novoselov *et al.* [2]. It can also be defined as a single layer of its 3D counterpart, graphite, or as the basic building block for other carbon-based structures, such as 1D carbon nanotubes [3] and 0D fullerenes [4]. The crystalline structure of graphene is a lattice of carbon atoms with strong in-plane sp^2 bonds. Since each carbon forms three bonds to neighboring carbon atoms and the angle between each sp^2 bond is 120°, the atoms organize in a characteristic honeycomb lattice. Out of plane, the graphene layer only interacts with other materials with weak van der Waals forces. Due to its confinement, it exhibits various interesting properties, such as ultrahigh carrier mobility and high thermal conductivity. The strong in-plane bonds also give graphene a high strength and stiffness. In addition, the lack of out-of-plane dangling bonds makes graphene a very inert material.

The high carrier mobility of graphene makes it a very promising material for electronic applications. Nevertheless, its zero bandgap limits its possibilities. However, the properties of graphene and 2D materials in general, are highly dependent on their surroundings. Changing the substrate, modifying the number of layers, or adsorbing molecules atop leads for example to changed properties of graphene. An example can be found in [5], where Jørgensen *et. al* reported a change in the graphene band-gap after adsorbing atomic hydrogen atop. Similar intercalation of atoms or molecules beneath graphene can be used to dope graphene and thereby change its properties [6].

Isomorphic to graphene we can find hexagonal boron nitride (h-BN). It consists of a single layer of alternating boron and nitrogen atoms also arranged honeycomb network with each B or N atoms sp^2-bonded to the other atom. Contrary to graphene, boron nitride is an insulator with a direct band gap in the ultraviolet range (5.97 eV), which makes it a promising high-quality dielectric material for 2D electronic applications. At the same time, its atomically smooth surface, relatively free of dangling bonds and trapped charges, makes h-BN a suitable substrate for graphene and other 2D materials [7].

Among all the applications for Gr and h-BN, one of the most attractive is the possibility of constructing van der Waals structures by controlled stacking off different 2D materials. The stacked structure of graphene/h-BN allows the fabrication of graphene-based electronic devices, while the in-plane heterostructures can be used in the construction of atomically thin integrated circuits. The combination of graphene and hexagonal boron nitride in a stacked heterostructure has also been proven to enhance some of the properties of graphene. For example, Giovannetti *et al.* showed that a band-gap was induced in graphene aligned to a two-dimensional h-BN substrate [8]. Dean *et al.* also showed that graphene devices on h-BN substrates have mobilities and carrier inhomogeneities that are almost an order of magnitude better than devices on the commonly used SiO_2 substrate [9]. Nevertheless, the direct manufacture of Gr/h-BN heterostructures remains a technical challenge for the direct application of these devices.

Several growth methods have been employed to synthesize graphene and hexagonal boron nitride. A very common approach is mechanical and chemical exfoliation of the two-dimensional layer followed by a transfer to the desired substrate. Although crystals of excellent quality can be produced in this way, these methods are limited to small samples (a few millimeters) and they are therefore used mainly in research. In contrast, the so-called bottom-up routes offer the advantage of synthesizing large area samples. In this case, the 2D film is grown through physical or chemical methods. A popular method for large-scale production of 2D materials is Chemical Vapour Deposition (CVD). It is based on dosing a precursor gas on a hot, catalytically active surface. The precursor dissociates on the surface (see figure 1a) and the atoms diffuse around on the substrate, form bonds with each other, and eventually a 2D crystal is formed (figure 1b). The main limitation of this technique is the need of a catalytically active substrate. This impedes, for example, the implementation of two-dimensional materials on the desired substrate for electronic devices, which is usually not catalytically active, or the direct growth of the Gr/h-BN stacked structures discussed above.

Until the present date, the stacked structures have been mainly achieved by top-down techniques such layer-by-layer transfer of 2D sheets of the different materials [1, 7]. Only recently, other methods for direct growth are starting to appear. For example, Yang *et al.* reported the epitaxial growth of single-domain graphene on h-BN by a plasma-assisted deposition method [10]. It consists on dissociating the precursor molecule with a remote plasma source enabling the growth of the crystalline layer on thin BN films (20 to 120 nm thick) supported by SiO_2/Si. By this method the authors obtained a continuous single-crystalline monolayer of graphene with a size limited only by the size of the h-BN substrate. In addition, the graphene grown was free from grain boundaries and its rotation was locked at a to that of h-BN. These results indicate that the future of Gr/h-BN stacked heterostructures and their applications will be related to the development of these direct growth techniques.

In this thesis we present a similar but simpler method for direct growth of 2D material atop a non-catalytic substrate; *Electron Assisted Growth*. In the past, atomic hydrogen has been produced by dissociation of molecular hydrogen using a hot tungsten filament placed near the sample [11]. We reused that concept and applied it to 2D materials growth. In the same way as the electrons emitted from the hot tungsten filament dissociate H_2 molecules, we used them to dissociate the borazine molecules needed to grow the h-BN. Figure 1c shows a sketch of the experimental setup. Compared to the work by Yang *et al.* introduced above, our technique offers the advantage that can be used in any UHV setup with no need for a plasma source. In addition, we will use our technique to probe if it is possible to grow a stacked heterostructure composed by one-atom-thick crystalline layers and not thin films, as the h-BN/Gr structures reported by Yang *et al.*.

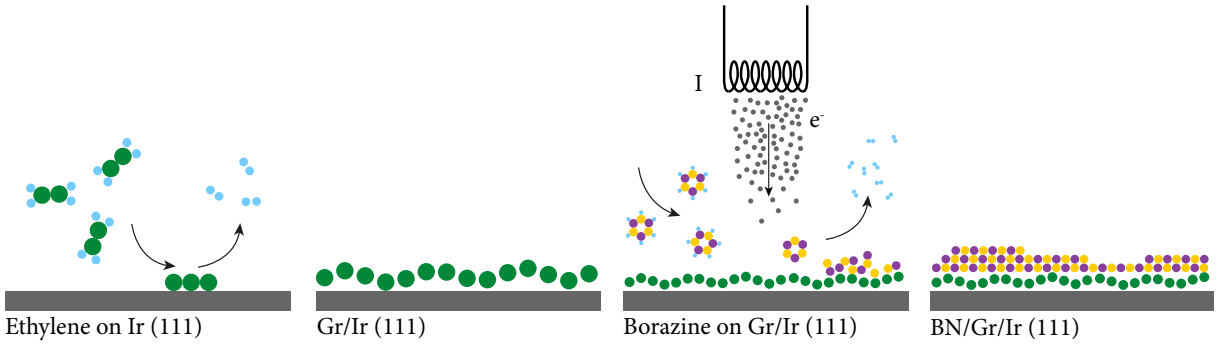

Figure 1: Simplified description of the experimental process: The first two steps correspond to the growth of 1 ML Gr on iridium (grey block) with Chemical Vapor Deposition (see section 3.1.2 for more details about the graphene growth process). The third step exemplifies how we dose the precursor gas for h-BN (borazine) at room temperature with the assistance of the molecule cracker. The final step corresponds to a possible surface after the dosing; multilayer of BN atop Gr/Ir(111).

In order to prove the performance of this method, we will use electron assisted growth to form an h-BN film, atop an inert 1 ML graphene film supported on Ir(111). Once grown, Scanning Tunneling Microscopy (STM) will be used to characterize the structure of the h-BN films, while X-Ray Photoemission Spectroscopy (XPS) will be used to probe the different elements and their bonding configuration. Altogether, the interplay of the two techniques will yield a quite complete picture of the system studied.

The importance of this project is two-fold; First of all, we aim to prove the viability of a new growth method to grow 2D materials. Secondly, by using our technique to grow h-BN on graphene, we seek to gain fundamental knowledge of the growth and structure of such an interesting heterostructure.

2 Experimental techniques

In this section, the different experimental techniques used for this thesis will be presented including both a theoretical description of the working principles and a description of the specific experimental setups used.

2.1 Scanning Tunneling Microscopy

Scanning probe techniques such as Scanning Tunneling Microscopy (STM) have revolutionized both fundamental and applied studies of solid surfaces by providing highly localized structural and electronic information of surfaces. The scanning tunneling microscope was invented by G. Binning and H. Rohrer in 1982 and they both received the Nobel prize for their work four years later [12]. Today the STM is a standard tool in surface science laboratories with thousands of systems worldwide. The strength of scanning tunneling microscopy is its capability to provide real space images of the surface with a resolution about 1 Å in the surface plane and as low as 0.1 Å orthogonal to the surface. STM has been used in this thesis to image graphene/Ir(111) and BN/graphene/Ir(111) at different steps in the growth procedure.

STM is based on the tunneling current of electrons between a sharp tip and a conductive sample. The energy necessary to remove an electron from a solid is the so-called work function of the material, ϕ, also defined as the difference between the Fermi level and the vacuum level of that material. To move this same electron from one solid (the sample, for example) to another solid (the tip) it has to overcome the vacuum barrier between the two materials. Nevertheless, if the distance that separates them is smaller than the decay length of the electronic states, the electrons can cross the barrier by quantum mechanical tunneling.

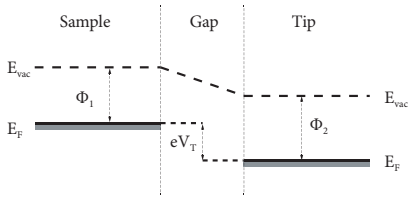

Figure 2: Simplified energy level scheme of a tunnel barrier with a negative bias, V_t, applied. E_{vac} and E_f correspond to the vacuum and fermi levels respectively.

As can be seen in figure 2, the bias V_t leads to an offset of the fermi levels on each side of the barrier, and a net tunnel current is thereby established between the sample and the tip. Using the Wentzel-Kramers-Brillouin approximation this current can be described as follows:

$$I = \rho_1 \rho_2 V_t exp(-2z\sqrt{m(\phi_1 + \phi_2)/\hbar^2}) \tag{2.1}$$

Here, ρ_1 and ρ_2 refer to the local densities of states for the tip and the sample[1]. V_t is the bias applied, and ϕ_1 ϕ_2 are the different work functions. $\hbar$ is Plank's constant, m is the mass of the electron, and z is the distance between the tip and the sample. From the expression 2.1 we see that the tunnel current measured is strongly dependent on the separation distance, z. This strong dependence is exactly what gives the STM its extreme height resolution, in the order of 0.1 Å. In the same expression, we can see that the measured current has also a strong dependence with the local densities of states. The densities of states are confined around each atomic nuclei. Because of that, with STM we can achieve atomic resolution [13].

Obtaining a highly localized tunnel current requires a very sharp tip; ideally terminated by an atom or a small cluster of atoms. For STM in vacuum systems, it is common to use electrochemically etched tungsten (W) tips. The position of the tip both in-plane (x,y) and out-of-plane (z), is controlled by piezo-elements with picometer resolution (see figure 3).

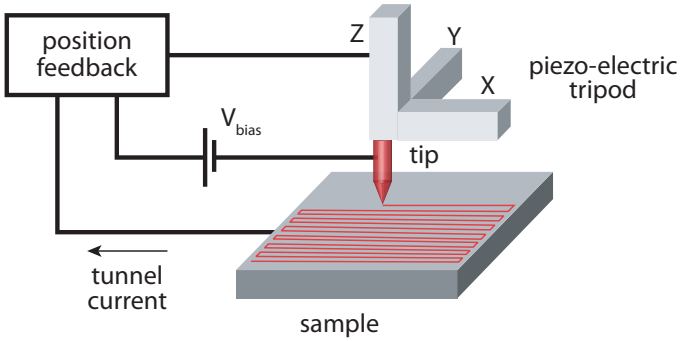

Figure 3: Schematic setup of a scanning tunneling microscope. The scanning movement is realized by changing the voltage over the x- and y-piezos. At the same time, either the tunneling current or the change in the z-piezo is monitored to compose the STM image.

The images are obtained with the tip scanning the sample in a line-by-line fashion while a constant bias is applied. The STM images included in this thesis were acquired in a constant current mode; The tunneling current is measured at each pixel of the image and compared to a chosen current set point. If the current measured is higher or lower than the reference value, the sample-tip distance is corrected by applying the appropriate voltage to the z-piezo element (see figure 3). With this closed-loop operation, it is possible to maintain the current constant while the trajectory z(x,y) is used to create a topological map of the surface. More accurately, as the local density of states varies significantly across the surface, what is being generated is a map of a particular charge density contour above the surface. By changing the bias voltage or due to atomic changes in the tip we can access electrons in different local charge densities, therefore especific elements will become more or less visible. See in figure 4, the comparison of two different STM images of the same location in the sample. The surface shown is a monolayer of graphene on Ir(111) after

[1]Simplified to constant values for the approximation

depositing 300L of Borazine and annealing at 1323 K. In figure 4a, the graphene substrate can be seen underneath the adsorbates in the top left corner. Because of a change in tip, the same feature can not be seen in the image in figure 4b.

(a) *(b)*

Figure 4: Comparison of two different charge density contours of the same location in the sample. Scanned surface: Boron Nitride deposited on Gr/Ir(111) with electron assisted growth and annealed at 1323 K. a) The graphene substrate is visible underneath the adsorbates (red circle). b) Due to a change on the morphology of the tip, the graphene is not visible anymore.

During the tunneling contact, the distance between the sample and the tip is around 1 nm. Therefore, any mechanical vibration will affect both the tunneling contact and the tip can in a worst case scenario crash into the surface. In order to avoid such vibrations, the microscope head is built as compact as possible, integrating both the tip and the sample on a rigid platform. With this approach, we obtain a high resonance frequency for oscillations of the tip relative to the sample. At the same time, the entire microscope is isolated against external vibrations by being suspended by soft springs. The goal is to achieve a maximum mismatch between the mechanical modes of the soft suspension system and the high resonance of the stiff microscope head. In addition, efficient vibration damping is achieved by eddy current damping system. Altogether, these precautions effectively shield the STM against outside vibrations.

It is important to notice that the electrons measured with STM are valence electrons. Therefore, even though we are able to image different density of states at different energies, STM images cannot provide chemical information about the surface scanned. In order to obtain a complete description of the studied surface, parallel measurements have to be performed with a chemically sensitive technique. In our case we used X-Ray Photoemission spectroscopy, that is discussed in section 2.2.

The STM images included in this thesis were recorded in two different STM setups. For the h-BN/Ir(111) system, the images were acquired at the STM lab in the MaxIV laboratory, Sweden, with a ScientaOmicron VT-STM XA STM. For the Gr/Ir(111) and BN/Gr/Ir(111) measurements, the STM employed was a ScientaOmicron STM1, part of Lund University, in the Synchrotron Radiation Department. All the measurements were performed at room temperature.

2.2 X-Ray Photoemission Spectroscopy

To complement the STM images, X-Ray Photoemission Spectroscopy (XPS) measurements were performed. XPS is one of the most common techniques for surface characterization. It was developed by K. Siegbahn and his group in the late 1960's. Later in 1981 he received the Nobel prize to "acknowledge their extensive efforts to develop XPS into a useful analytical tool" [14].

The XPS technique is based on the photoelectric effect; when a sample is irradiated with monochromatic X-ray radiation (from a laboratory source or from a synchrotron) the emission of a core level electron is induced. While the penetration depth of the incident photons is of the order of hundreds of nanometers, the short mean free path of electrons in solids makes XPS a surface-sensitive method. XPS requires good vacuum conditions during the measurements since the emitted photoelectrons can be scattered by the gas phase molecules. The spectra obtained will reflect the different elements present in our sample, as well as their chemical environments. Therefore providing very valuable information about the system studied in this thesis.

2.2.1 Core-level binding energies

The binding energy of a core-level electron is characteristic for every element. Therefore, an XPS survey spectrum can be used to accurately determine the chemical composition of the surface and near-surface region of a sample. The kinetic energy of the emitted electrons will be equal to the incident photon energy minus the energy required to remove the electrons from the core level where they originate (binding energy). Therefore, knowing the incident photon energy, $h\nu$, and the measured kinetic energy (E_{Kin}), the binding energy of the electrons ($E_{Binding}$) can be determined:

$$E_{Binding} = h\nu – E_{Kin} = E(N-1) - E(N) \tag{2.2}$$

From the perspective of energy conservation, the binding energy can also be defined as the difference between the total energy of the system with N-1 electrons minus the energy of the system with N electrons. With this definition, it is evident that both the initial and the final state contribute to the resulting binding energy. Shifts in the binding energy due to changes in the local environment of an atom that originate from E(N) are called *initial state effects*, while shifts originating from E(N-1) are denoted as *final state effects*.

Initial state effects are caused by a change in the local potential. For example, if an atom forms polar bonds that remove part of its valence density of charge, the electrostatic potential of the atom will become more attractive. A more positive electrostatic potential implies that the total energy of the electron system is lower. Therefore, the energy necessary to remove a core-level electron becomes higher. This is the case of the nitrogen and boron core levels when the crystalline h-BN structure is formed. The in-plane bonds between boron and nitrogen in h-BN are polar bonds. Since the nitrogen atom is more

electronegative than the boron atom, the valence charge is displaced towards the nitrogen. This implies that boron in h-BN has a more attractive electrostatic potential than boron in atomic form. Nitrogen, on the other hand, will have a more repulsive potential. Because of those changes, the binding energy measured for boron in h-BN is higher than the binding energy for atomic boron (190,18 eV[2] and 188 eV[3] respectively). The contrary happens with nitrogen, the binding energy in h-BN is lower than nitrogen in atomic form (397.92 eV[2] and 409.9 eV[3]). Since the binding energies of core electrons reflect the nature of the chemical bond, these shifts are called *chemical shifts*. It is worth mentioning that the relation between the binding energy and the chemical environment of an atom is unique only if the coordination number[4] is the same. This is especially important when analyzing surface layers or 2D materials because surface atoms have a lower coordination number than atoms in the bulk. Therefore, the electrostatic potential resulting from neighboring atoms is less attractive for surface atoms than for atoms in the bulk. This means that core electrons from surface atoms will have a smaller binding energy than core electrons from the bulk. The shifts in the binding energy for surface atoms are referred as *surface core-level shifts*, and are comparable in magnitude with the chemical shifts. In figure 5 the spectrum of Ir 4f is shown. Both Ir $4f_{5/2}$ and Ir $4f_{7/2}$ core levels are clearly visible, centered at 63.8 eV and 60.8 eV respectively. In addition, the surface components and the bulk components can be clearly distinguished for each spin-orbit split component.

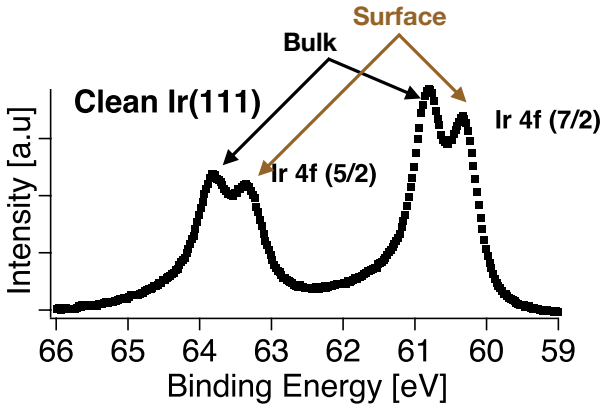

Figure 5: XPS measurements of Ir 4f core levels on a clean Ir(111) sample with an incident photon energy of 130 eV. Four components can be distinguished, the bulk and surface component of Ir $4f_{5/2}$ (63.8 eV and 63.3 eV respectively) and the bulk and surface component of Ir $4f_{7/2}$ (60.8 eV and 60.3 eV respectively).

Final state effects are all the contributions to the binding energy not included in the initial state effects. They will reflect the capacity of the electron system to screen the core hole created in the photoemission process. The more effective the screening, the lower the energy of the final state (E(N-1) in equation 2.2) and therefore the lower the binding energy. For

[2]Value measured in 1 ML h-BN. See section 3.2.1 for more details
[3]Tabulated value from [15]
[4]The coordination number is the total number of neighboring atoms of a central atom.

transition metals, like iridium, the screening involves a relocation of electronic charge from the surrounding atoms to the atom with the core hole, that requires the filling of the empty states right above the fermi level (as they require the least energy). At the surface, the density of states around the fermi level is higher, therefore core holes in surface atoms will be more effectively screened and the binding energy of the electrons will be reduced by this effect [11].

2.2.2 Features and lineshapes in XPS

Various factors influence the shape of a core level photoemission peak. First of all, the core-hole that the incident photon creates has a particular lifetime (τ) which is dependent on how quickly the hole is filled by an electron from another shell. From Heisenberg's uncertainty principle, the finite lifetime will produce a Lorentzian broadening of the photoemission peak. Secondly, Gaussian broadening due to the finite resolution of the beam and the electron analyzer always occurs. Often the magnitude of the Gaussian and Lorentzian broadening is comparable and it is, therefore, necessary to convolute Gaussian and Lorentzian line shapes. The numerical convolution of Gaussian and Lorentzian line shapes are called Voight line shapes while approximate analytical functions approximating the real convolution are called pseudo-Voight functions. In addition, the excitation of phonons generated during the photoemission, the vibrational excitations that usually accompany the electronic transitions and the changes in the surface potential will add an extra Gaussian broadening of the peak.

As this research is centered on 2D materials, it is important to mention that the width of the peaks will be also related to the corrugation of the 2D layer [16]. The corrugation is due to the lattice mismatch between the top layer and the substrate. Depending on the relative position of the atoms of the 2D crystal and the atoms of the substrate, the interaction force between them will vary, implying then a change in the bond length[5]. For a strong interaction between the 2D layer and the substrate the corrugation will increase, meaning that electrons from atoms with different bonds will be included in the same photoemission peak. This will cause an increase of the peak width. On the other hand, for very weak interactions or almost free-standing crystals, the corrugation decreases and the correspondent core level peak becomes sharper.

In addition, the creation of electron-hole pairs around the Fermi level will make the line shape of the peak asymmetric, adding a tail towards high binding energies. This is especially important for metals because of the continuous density of states in that region. In other words, because of the available valence levels right above the Fermi level, the photoelectron generated from the core level can lose some energy by generating a core-hole around the fermi level. This electron with less kinetic energy creates the characteristic tail at higher binding energies. This asymmetry is clearly visible in the C 1s spectrum included

[5]For more details about the corrugation of Gr and h-BN on Ir(111) see sections 3.1.2 and 3.1.3

in figure 6. For comparison, the C 1s core level has been fitted with a symmetric and an asymmetric Voight function, respectively.

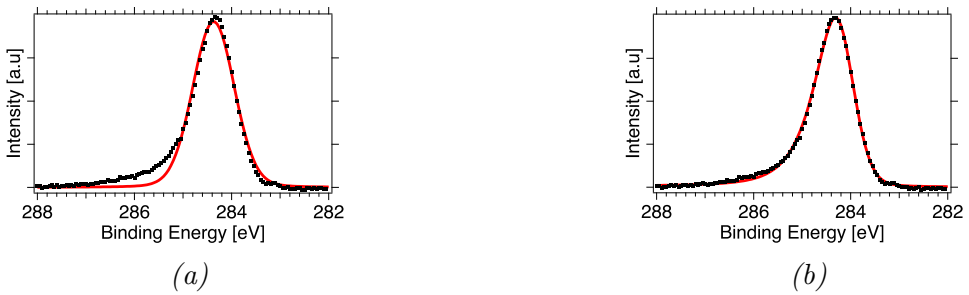

Figure 6: XP spectra of C 1s measured at 390 eV on 1 ML Gr/Ir(111). a) Spectrum fitted with a symmetric voight function. b) Spectrum fitted with an asymmetric voight function. The accuracy of the asymmetric fitting is clearly superior than the symmetric one.

Finally, we will choose an incident photon energy according to the depth that needs to be proben. The penetration depth of the incident photons is of the order of hundreds of nanometers, but the electrons emitted have a very short mean free path in solids (λ). As can be seen in figure 7, the mean free path for most elements fall on a universal curve with a minimum around a kinetic energy of 50 eV. Therefore, by changing the incident energy accordingly, we can tune the surface sensitivity of the technique.

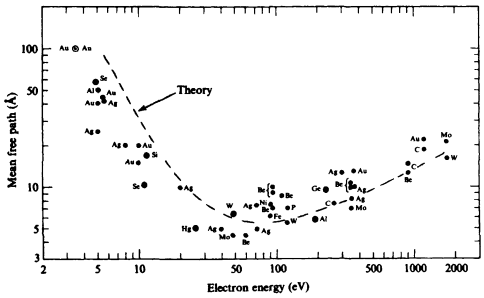

Figure 7: Universal curve for the electron mean free path (in Å) as a function of the kinetic energy (eV). Reproduced from [17].

2.2.3 The light source

Conventionally, x-rays are produced by accelerating electrons in a vacuum and bombarding a target material with them. The incident electron flux will excite core-level electrons and eject them from their inner shells. Fluorescence decays to fill the core holes and as a result x-rays with well-defined photon energy will be emitted. However, traditional sources lost some of their importance when synchrotron sources that cover the entire spectral range became available.

Synchrotron radiation is produced when electrons at relativistic velocities are circulating in an orbit defined by a magnetic lattice (storage ring). As the electrons are deaccelerated to turn in the circular ring, they emit electromagnetic radiation. The radiation is emitted in a narrow cone in the forward direction of the moving electrons. It has a continuous spectrum and its polarized in the plane of the ring. The energy range available goes from infrared to hard x-rays. The exact energy spectrum depends on the specific synchrotron facility and the beamline of interest. The typical brilliance achieved with a bending magnet is five orders of magnitude higher than for an x-ray tube. To obtain an even higher brilliance and photon flux, dedicated magnetic devices can be inserted in the straight sections of the storage ring. They consist of a periodic array of magnets designed to make the electron beam oscillate around the straight path that they would have followed without the magnetic array. At each magnetic pole, the electrons make a sharp turn and spontaneous radiation occurs. Depending on the exact insertion device, the brilliance obtained is between two to six orders of magnitude higher than the one obtained from the bending magnets [18].

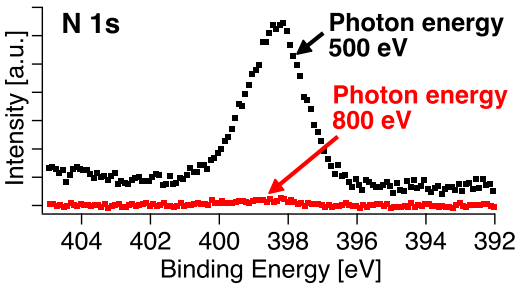

Figure 8: XPS measurements of N 1s core level on a 1 ML Gr/Ir(111) after dosing 300 L of Borazine with the molecule cracker. The difference in intensity of the N 1s peak is clearly visible for different incident photon energies.

The main advantage of synchrotron sources is that they combine high photon fluxes with tunability in a wide spectral range. We have already seen that the incident photon energy can be tuned to optimize the surface sensitivity of XPS. At the same time, the measured intensity will also depend, among other factors, to the cross-section of the core level measured[6]. The cross-section will then depend on the incident photon energy with a dependence that varies with the core level measured. Therefore, by tuning the energy of the photons one can optimize both the depth probed and the cross section to photoemission from a particular core level. See in figure 8 the comparison of the N 1s spectra obtained with the optimized photon energy of 500 eV and the same spectrum obtained with an incident photon energy of 800 eV. For that sample, the nitrogen atoms were placed on the surface. Therefore, by measuring with a photon energy of 800 eV we were both probing the wrong depth and with an energy not optimized for the cross-section of the nitrogen.

[6]See section 3.2.1 for more details about the intensity of the intensity of the photoemission peak.

The measurements included in this thesis have been performed at the ASTRID2 Synchrotron in Århus, Denmark. The energy of the circulating electrons in ASTRID2 is 580 MeV, the horizontal emittance is 12 nm, and the source is optimized to produce photons with energies from a few eV to 1 keV energy range. Beam lifetime is effectively infinite due to the top-up mode. The diameter of ASTRID2 is 15 m [19].

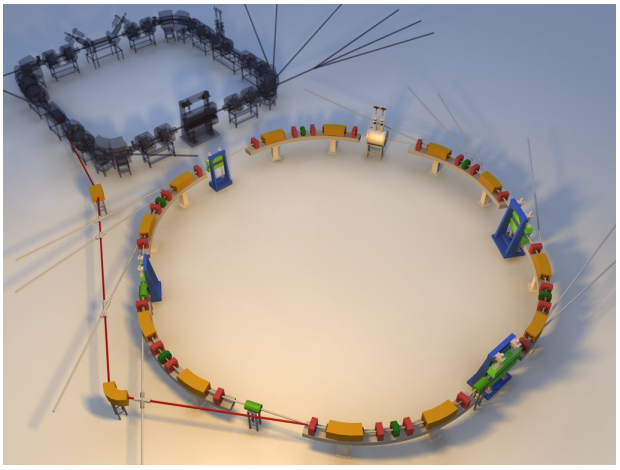

Figure 9: Render of ASTRID2 Synchrotron in Århus, Denmark. In the back the old storage ring, ASTRID can be seen. Now ASTRID serves as an accelerator for the electrons injected in ASTRID2.

2.2.4 The beamline

The experiments were performed at the AU-MATLine, a material science focused beamline. Its core elements are a Scienta electron energy analyzer and a SX-700 monochromator. With the help of a multipole wiggler, the usable energy range is from 20 eV to 1000 eV. MATLine offers ultraviolet photoelectron spectroscopy (UPS), X-ray Photoelectron Spectroscopy(XPS), photoelectron diffraction (PED) and near edge X-ray absorption fine structure spectroscopy (NEXAFS) measurements [20].

3 Results and discussion

Earlier in this text, we have introduced graphene and hexagonal boron nitride, the two 2D materials used in this work. Together with their basic descriptions, the main approaches for manufacturing those 2D layers were presented. Among all the techniques existent for manufacturing 2D materials, Chemical Vapor Deposition was described as the most promising technique for producing large areas of high-quality crystals. Because of that, all the 2D layers used in our experimental results have been grown using CVD or variations of this technique.

We used three different approaches for growing Gr and h-BN: (i) Chemical Vapor Deposition, (ii) Temperature Assisted Growth (TPG), a very close variation of the CVD approach, and (iii) Electron Assisted Growth, the novel method presented with this work. CVD and TPG were used to grow the graphene layer on an iridium substrate used both as a reference sample and as the substrate for our final experiments. A reference sample of h-BN on iridium was also grown with TPG. Finally, the Electron Assisted growth technique was used to grow a BN layer atop a 1 ML graphene substrate.

Therefore, the results obtained will be organized as follow. First, we will explain in detail the CVD and TPG growth techniques, and we will present the results obtained when using them for growing Gr and h-BN on iridium (subsection 3.1). The next section, 3.2.1, will focus on describing the Electron Assisted Growth technique and the results obtained when attempting to grow a layer of boron nitride atop a graphene substrate.

3.1 Growth of 2D materials on iridium substrate

3.1.1 The substrate: Ir(111)

We used iridium as a substrate for the growth of graphene. Similar to its neighbor in the periodic table, platinum, surfaces of iridium are very active catalysts for a number of catalytic reactions including the CO oxidation and the dissociation of hydrocarbons. In addition, it has a very high melting point of 2700 K, an interesting property as Gr and h-BN will need high temperatures to crystallize. Iridium is an fcc metal with a unit cell as shown in figure 10. For my experiments, I used the Ir(111) surface which has a hexagonal unit cell, defined by the vectors $\vec{a}$ and $\vec{b}$, both with a length of 2.71 Å, and an angle between them of 120° as can be seen in figure 10.

Before the graphene growth, a clean iridium surface had to be produced. To do so, the iridium was first prepared by cycles consisting of Ar^+ sputtering at room temperature ($2 \cdot 10^{-5}$ mbar) followed by annealing at 1170 K in an oxygen atmosphere ($5 \cdot 10^{-7}$ mbar) and finally vacuum annealing at 1300 K.

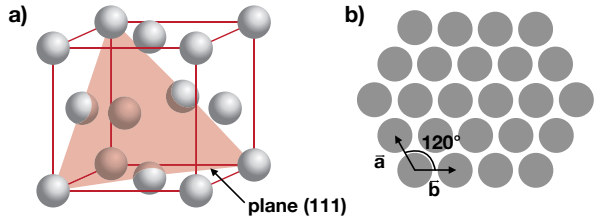

Figure 10: a) Schematic respresentation of a Face Centered Cubic unit cell (fcc), with the plane (111) highligted in red. b) Simplified atomic structure of the top layer of the plane (111).

3.1.2 Graphene growth on Ir(111)

In order to demonstrate the functionality of the Electron Assisted Growth technique, we need an inert substrate. One of the properties of graphene is its inertness, therefore we can neutralize the catalytic power of iridium by covering it with a full monolayer [21]. As iridium is a very catalytically active substrate, it is essential that the graphene film fully covers the surface. Otherwise, the precursor molecule could on patches of bare metal and would be impossible to probe the effect of the electron assisted dissociation. Furthermore, it is also important to notice that different graphene domains, domain boundaries or defects in the graphene film could also affect our results by changing the characteristics of the material grown atop or creating preferred nucleation spots [22]. Therefore, to ensure the reliability of our results, we need to grow a full monolayer (ML) of highly ordered graphene.

To achieve a 1 ML graphene film that covered the entire Ir(111) crystal while maintaining the high quality of the 2D crystal produced, we used the combination of the two growth techniques mentioned above; Temperature Programmed Growth and Chemical Vapour Deposition. By first using TPG we obtain highly ordered flakes that act like seeds for CVD growth, which follow their alignment.

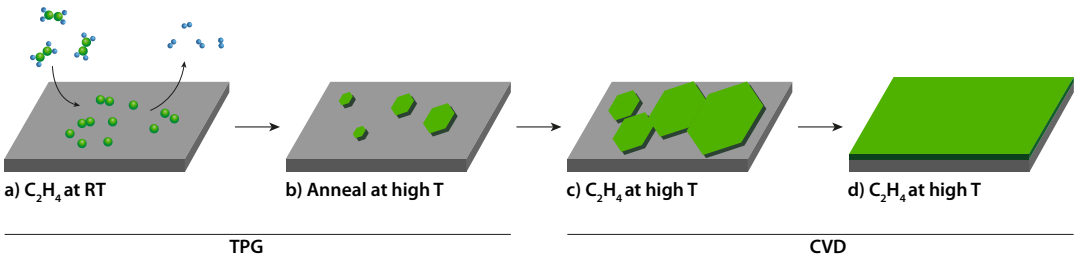

Figure 11: Schematic description of thermal decomposition of hydrocarbons on a catalytic substrate with the following crystalization in a 2D layer. The steps a and b correspond to TPG growth while c and d describe the CVD growth. Figure adapted from [23].

The Temperature Programmed Growth method is based on the adsorption of the precursor on the metal substrate at room temperature. In our case, we used Ethylene (C_2H_4) as a precursor. By heating up the surface the precursor molecule is decomposed, the hydrogen

desorbs from the surface and the carbon atoms remain adsorbed (figure 11a). If we provide enough energy, the adsorbed carbon atoms will start diffusing around the surface, forming small graphene islands (figure 11b). The order, shape and the size of the flakes increase with the annealing temperature; Several rotational domains for Gr on Ir(111) are possible, R0° is the most common one but also R14°, R18.5°, and R°30 can be formed (see figure 13)[23]. By annealing the sample at high enough temperatures (above 1350 K), we ensure that all the flakes align to the most energetically favorable rotation, R0° (see figure11c).

Although TPG can be used to form higher coverages, a perfectly closed monolayer is impossible to achieve. For each annealing cycle, the remaining bare Ir(111) surface is only reduced by 20%. In contrast, with CVD we can achieve a faster growth rate by dosing higher pressures of the precursor while maintaining the substrate hot (1170 K). Nevertheless, the growth temperature for CVD cannot be as high as the temperature needed for the R0° alignment of graphene. In that case, the precursor would desorb as soon as it reached the surface, making it impossible to achieve one single rotation domain with CVD. Therefore, by combining TPG and CVD we obtain the advantages of both techniques; a highly ordered full monolayer of graphene. For the TPG growth, we dosed 100 L (10^{-6} mbar for 100 s) of ethylene at room temperature followed by flashing at 1320 K to align the flakes. For the subsequent CVD step we dosed 120 L (10^{-7} mbar for 1200 sec) of ethylene at 1170 K. As the presence of bare metal is necessary for both methods to dissociate the molecule, we can ensure that the growth process will limit itself to one monolayer.

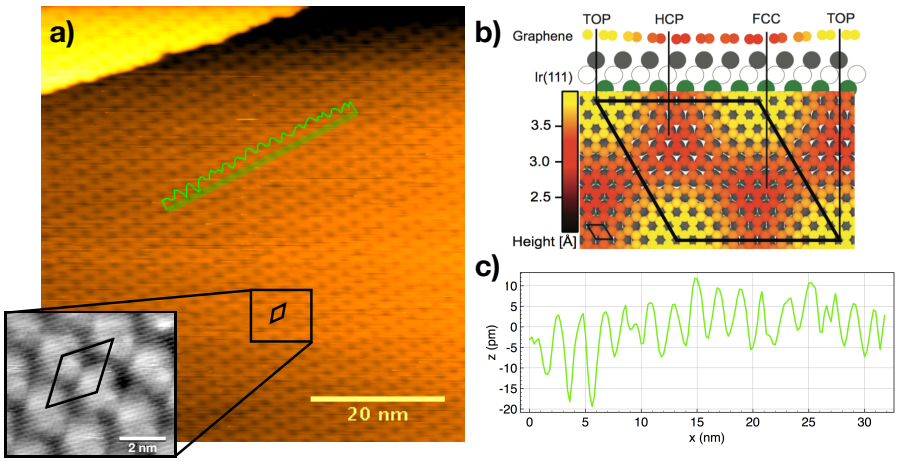

Figure 12: a) STM image of a full monolayer of defect-free and highly ordered graphene on Ir(111). The edges of the substrate are visible together with the Gr moiré pattern. Size 100×100 nm. Inset: STM image with an atomic resolution of graphene on Ir(111). Both the hexagonal atomic structure and the moiré pattern are visible. b) Ball model of graphene on Ir(111). We can see how depending on the relative position of the carbon atoms with the iridium atoms, the attraction forces differ, which causes the corrugation on the 2D layer. Visible in black in a and b the moiré unit cell represented in the ball model. The periodicity of the moiré unit cell of graphene on Ir(111) is 25.3 Å. c) Height profile along the green line in image a.

Representative STM images of the graphene grown on Ir(111) can be seen in figure 12a. The pattern clearly visible covering the whole image is a moiré pattern which originates from the lattice mismatch between iridium and graphene; 2.72 Å and 2.46 Å respectively. Because of this mismatch, the relative positions of the graphene unit cells are not always the same. Depending on this relative position, the interaction between the substrate and the graphene unit cell will be different, generating a corrugation in the graphene layer that can be seen in the inset c of figure 12. In addition, due to the small difference in lattice constants (about 10%), the relative positions of the carbon atoms with respect to the underlying iridium atoms are repeated for every 10 atoms. This generates a repetitive pattern that is represented by a moiré unit cell (black rhombus visible in figure 12a and b).

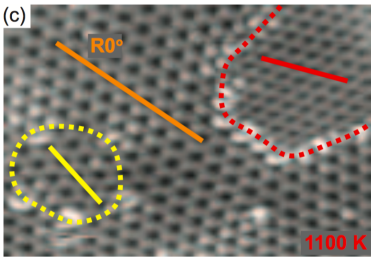

Figure 13: graphene on Ir(111) grown by CVD at 1100 K. Although R0° is the main orientation, small regions with different rotations are present. Image reproduced with permission from [23].

The moiré pattern is also visible in the STM images with high magnification. An inset is shown in figure 12a. Here, we clearly see the atomic structure of the graphene and it is possible to verify the moiré unit cell contains 10 graphene unit cells. It is worth noticing that the corrugation on the graphene layer seems to be distorted, especially if compared to the model (figure 12b) or the general overview in figure 12a. This is due to "tip constructions" during the STM imaging. Not having an atomically sharp tip and instead off working with a double tip or an elongated one can create such effects in the final image[7]. In figure 12a and b we can also see that there is only one orientation of the graphene layer. As a reference, in figure 13 we can see an STM image of graphene grown on Ir(111) with 3 different rotation domains [23].

3.1.3 Hexagonal boron Nitride on Ir(111)

Hexagonal boron nitride is the crystal used to test the electron assisted growth technique. To do so, we want to grow it on an inert surface; the already introduced 1 ML of Gr/Ir(111). Before proceeding with that part of the experimental results, we need to characterize the growth of h-BN on Ir(111). The growth parameters obtained will guide us through the next step of our research. At the same time, the characterization of h-BN/Ir(111) will act as a reference to understand the results for h-BN/Gr/Ir(111).

[7]See section 2.1 for more details in STM imaging.

To obtain representative results of h-BN growth on Ir(111) we do not need to achieve a full coverage, therefore we used TPG to grow h-BN flakes. We used borazine as a precursor molecule. Borazine is a very common precursor for h-BN growth. Its chemical formula is $B_3H_6N_3$. It has a planar hexagonal structure, formed by alternated boron and nitrogen atoms. In the molecule, boron and nitrogen atoms are sp^2 hybridized, binding to two boron (or nitrogen) atoms and one hydrogen. The same type of bonds occur in the boron nitride crystalline structure. In that case, each boron (nitrogen) atom binds to three nitrogen (boron) atoms. This makes borazine a very good precursor gas for h-BN growth.

To obtain the boron nitride flakes we dosed 4 L ($4 \cdot 10^{-8}$ mbar for 100 s) of borazine at room temperature, followed by annealing at 1140 K. In figure 14a a representative STM image of the h-BN flakes is displayed. A representation of the moiré unit cell for h-BN on Ir(111) has also been included, together with the height profile of one of the h-BN flakes.

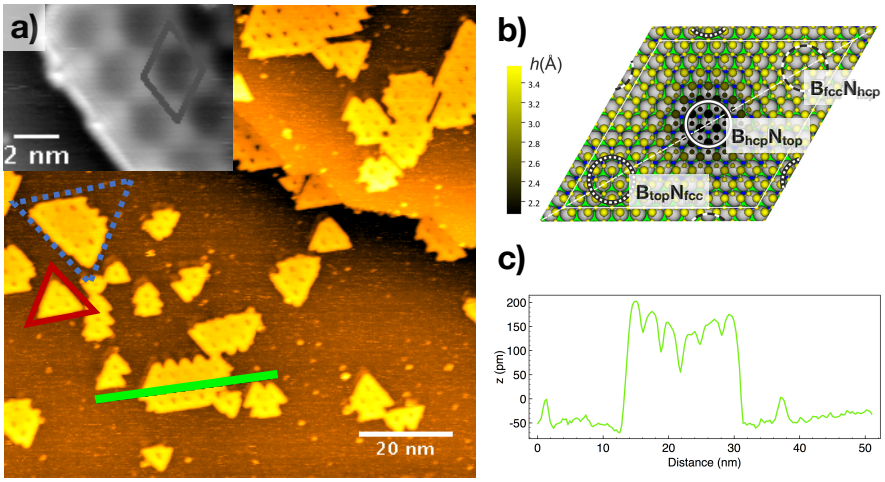

Figure 14: a) STM image of h-BN flakes on Ir(111). Two different rotation domains are visible (highlighted by red and blue/dotted triangles respectively). Inset: STM image with a near-atomic resolution of h-BN on Ir(111). The moiré pattern is visible and its unit cell represented in grey. b) Ball model of the moiré unit cell of h-BN on Ir(111). The periodicity of the moiré unit cell of h-BN on Ir(111) is 29.1 Å [24]. c) Height profile along the green line in image a. The moiré structure and the relative height of the flakes with respect to the iridium substrate are visible.

As we have seen in the graphene grown on Ir(111), h-BN on the same substrate also form a moiré pattern. In this case, the lattice mismatch between h-BN and iridium is around 9% (lattice constants of 2.48 Å and 2.72 Å respectively), and the pattern repeats itself for every 12 unit cells instead [24]. In figure 14b we can see the moiré unit cell superimposed in black on one of the h-BN flakes in the STM image. This unit cell corresponds to the unit cell shown in the ball model in figure 14b. An interesting feature of the h-BN flakes visible in the STM image in figure 14 is their characteristic triangular shape. This shape is due to the fact that boron atoms are more likely to bind to iridium atoms than nitrogen

ones [24]. This generates triangular flakes with 60° angles that follow the orientation of the iridium atoms in the substrate. As can be seen in figure 14a, two different domains (rotated by 180°) for the h-BN flakes are present in our sample. Contrary to the graphene case, neither of the domains is more energetically favorable than the other [24], therefore they will both be present when growing this 2D material.

Even though there are some differences in the specific parameters for growing graphene or hexagonal boron nitride, the overall concept is the same; using a catalytic substrate to dissociate the precursor molecule and anneal to form ordered structures. In both cases, the growth process is self-limited, as it is linked to the availability of uncovered substrate. In the following section, we will describe a variation of these growth techniques that bypass the need for a catalytic substrate. To illustrate its performance, we will present the results obtained when attempting to grow h-BN on top of a graphene-covered iridium substrate.

3.2 Electron assisted growth of h-BN on Gr

3.2.1 Step 1: Borazine dosing with the molecule cracker

As discussed in the previous sections, the in-situ growth of Gr or h-BN by the CVD process is impossible without the presence of a catalytically active surface that can dissociate the precursor molecule. Therefore, another method to dissociate the molecules is needed. In the past, atomic hydrogen has been produced by dissociation of molecular hydrogen using a hot tungsten filament placed near the sample [11]. Electrons emitted by the filament are then accelerated towards the sample by a positive bias applied to the sample, as exemplified in fig.15. In the same way that the atomic hydrogen is generated by a hot filament, we expect that the electrons emitted by the filament will collide with the precursor molecules and partly dissociate them. As a result, highly reactive radicals are formed just above the substrate. In contrast to the precursor molecules, we expect these radicals to bind very strongly to inert substrates, such as a Gr film. Altogether, the molecule cracker mimics the role of the catalytic substrate in CVD growth of Gr or h-BN.

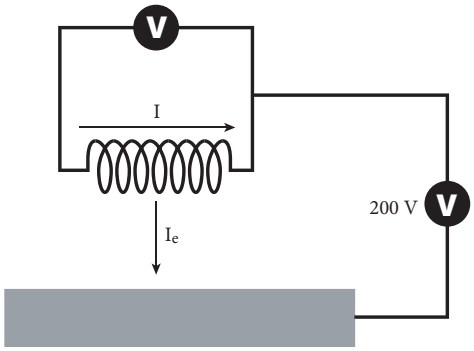

Figure 15: Schematic description of the experimental setup for the electron assisted growth of 2D materials. When a current, I, is applied on the filament, an emission current I_e is generated and redirected towards the sample by a bias of 200V between the filament and the substrate.

We do not expect any effect upon dosing borazine onto a complete Gr film as the catalytically active Ir(111) surface is fully covered by Gr. To verify this assumption, we dosed borazine onto a complete monolayer of graphene without operating the molecule cracker. Subsequently, we repeated the same experiment, this time with the tungsten filament on. Figure 16 shows N 1s, C 1s, and B 1s XP spectra of 1 ML graphene film exposed to 300 L of borazine, without and with the molecule cracker on. In addition reference spectra acquired on 1 ML h-BN grown on Ir(111) (bottom spectra) and 1 ML Gr on Ir(111) (second lower spectra) are included in the figure.

Starting with the reference spectra for h-BN, in fig.16 (bottom spectra) we observe clear N 1s and B 1s components as expected. The sharp N 1s peak at 397.92 eV (N_0) assigned to the nitrogen atoms in the h-BN lattice has binding energy in agreement with previously reported XP-spectra of h-BN on Ir(111) (397.58 eV and 398.46 eV in [24], 397.6 eV and

398.6 eV in [25], and 397.52 eV and 398.62 eV in [26]). Note that the reported values are composed of two different components. The main peak centered at lower energies representing the nitrogen weakly bound to the iridium, and another smaller peak at higher energies representing the nitrogen strongly bound. In our case, we have opted for a different approach. We used an asymmetric function to fit the data, with the peak centered at the binding energy correspondent to the weakly bound nitrogen (397.92 eV). At the same time, the asymmetry towards higher values reflects the presence of strongly bound nitrogen.

In the B 1s spectrum two peaks are observed (bottom spectrum fig.16c). The intense component at 190.18 eV (B_0) is assigned to the boron in the h-BN film, in agreement with the energies reported (189.92 eV and 190.72 eV in [24] or 190.5 eV in [26]). The second component, B_1 (188.53 eV) is attributed to atomic boron trapped in the iridium substrate. A component centered in a similar binding energy (188.9 eV) and attributed to boron adsorbed on iridium was reported by Valerius *et al.* in [25]. Most likely, boron atoms generated in previous experiments were trapped within the bulk of the iridium crystal. The high-temperature treatment used for the CVD growth of 1 ML h-BN then lead to the diffusion of B from the bulk to the surface.

We also measured the reference spectra for a pristine 1 ML graphene (see figure 16, second lowest spectrum). Here, we observe a single component C_0 located at 284.31 eV. The binding energy measured is in reasonable agreement with previously published XPS measurements of pristine graphene on Ir(111) (284.1 eV [5]).

As discussed above, we do not expect graphene or BN to grow on inert substrates. To confirm this expectation, we performed a test experiment in which we dosed 300 L of borazine ($1 \cdot 10^{-6}$ mbar for 300 s) at room temperature on a substrate fully covered by graphene. In figure 16 we observe no evidence for boron or nitrogen on the surface as the respective N 1s and B 1s spectra are featureless. Secondly, no visible changes are observed in the C 1s spectra. The C_0 component has the same width and binding energy as before the borazine exposure (see table 1). Altogether, this is clear evidence that the borazine molecules does not adsorb on graphene. It also confirms that the iridium substrate is fully covered by graphene, otherwise borazine molecules would have dissociated and adsorbed on the uncovered areas.

To determine the effect of the molecule cracker, an identical experiment was performed with the only difference being that the filament was on. The measurements acquired after dosing borazine with the filament on are shown in figure 16 (topmost spectra). In contrast to featureless spectra, we observed upon dosing without the filament on we now observe significant amounts of B and N on the surface.

Beginning with the N 1s spectrum, the peak measured after the electron assisted growth is centered at a slightly higher binding energy than the N 1s reference peak measured for 1 ML h-BN (398.31 eV and 397.92 eV respectively). The small difference in binding energy

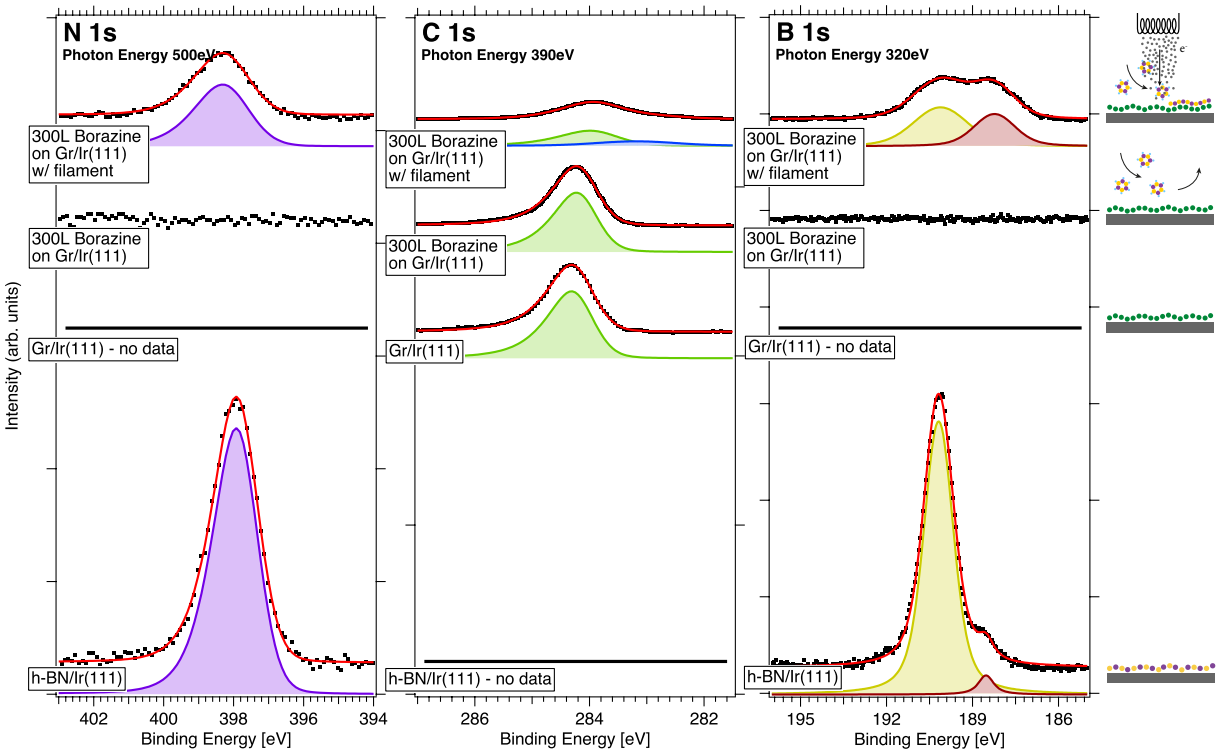

Figure 16: In situ XPS experiments. N(1s), C(1s) and B(1s) core levels obtained with an incident photon energy of 500 eV, 390 eV and 320 eV respectively. The two lower levels correspond to reference spectra of h-BN/Ir(111) and Gr/Ir(111) respectively. The two upper levels were obtained after dosing 300 L of borazine on 1 ML of Gr/Ir(111) at RT without and with the filament respectively.

is, however, not surprising. We expect that the deposited borazine molecules are fairly intact, most likely with hydrogen atoms left after the room temperature deposition. The reference spectra, on the other hand, was measured on an h-BN layer without hydrogen. Usachov *et al.* [27] reported a N 1s component at 397.7 eV labeled as molecular borazine chemisorbed on the iridium substrate. The same authors showed that the binding energy shifted to lower values (397 eV) with the formation of the h-BN crystalline structure. In our case, a similar difference is found if we compare the binding energy measured in h-BN (397.92 eV) with the one measured after the electron assisted dosing (398.31 eV). Therefore, we conclude that with the molecule cracker, we have deposited borazine radicals atop the graphene layer. Further, the larger width of the N 1s peak observed for BN grown by electron assisted growth (1.66 compared to 1.34 for 1 ML h-BN) suggest that we have a rather disordered structure with the presence of different radicals broadening the peak.

In the B 1s spectrum we encounter the same two components as observed for pristine h-BN. Nevertheless, their intensity ratio is now almost 1:1 (compared to 10:1 observed in h-BN). This observation suggests that the molecule cracker not only generate borazine radicals, but also a considerable amount of atomic boron. A more detailed analysis of this result is included in section 3.2.1. Returning to the B 1s spectra presented in figure 16, we

also see that the B_0 peak is broader (1.94 GFWHM now as compared to 0.9 for h-BN) but remains at the same binding energy (190.12 eV). In the same way, the B_1 component is broader but is centered at a similar binding energy (from 188.5 eV to 188.2 eV) (see figures 16c and 17b and table 1 for specific values). The fact that the component B_0 is centered at the same binding energy as observed for pristine h-BN, indicates that the borazine molecules and the borazine radicals bind to graphene mainly through the nitrogen atom. As a result of this C-N bonds, the binding energy of nitrogen is changed to higher values, while the boron B_0 remains unchanged. The broadening of both components is explained by the disordered borazine radicals, as discussed for the N 1s spectrum.

Altogether, the analysis of the N 1s and B 1s spectra obtained after the electron assisted growth suggests that we have a disordered structure of BN radicals and atomic boron atop graphene. It seems that the different borazine radicals bind to the graphene via the nitrogen atom. Most likely, the atomic boron is forming C-B bonds with the graphene film below. More details of the surface can be deduced from the analysis of the C 1s spectrum.

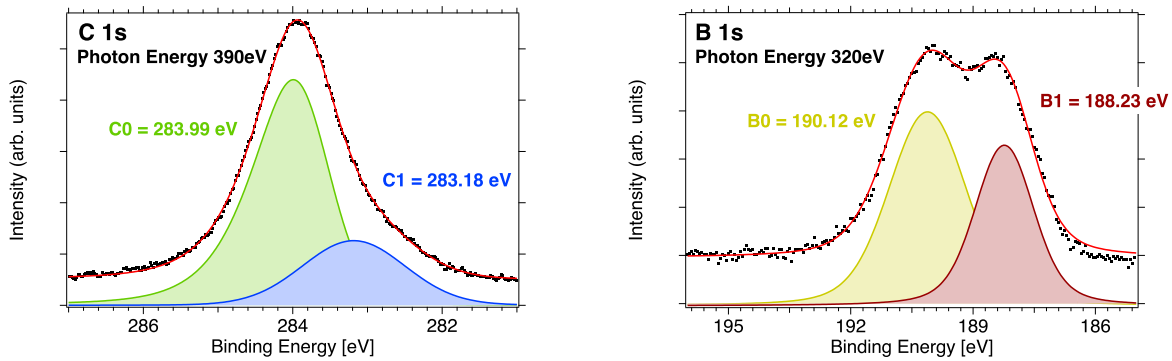

Figure 17: Detail of the C(1s) and B(1s) core levels after dosing 300 L of borazine on 1 ML Gr/Ir(111). a) C_0 (green) at 283.99 eV correspond to the Gr, while C_1 (blue) at 283.18 eV represent the carbon atoms binding to radicals deposited atop. b) B_0 (yellow) at 190.12 eV correspond to BN compounds, while B_1 (red) at 188.23 eV represents the boron in atomic form.

Compared to the pristine graphene spectrum, the C 1s main component, C_0, broadens from a GFWHM of 0.80 to 1.06 and shifts to lower binding energies (from 284.31 eV to 283.99 eV). At the same time, another component, C_1, appears at 283.18 eV (see detailed spectra in figure 17a). Like in the N 1s and B 1s spectra, these pronounced changes contrast with the results obtained without the filament where no change in the C 1s spectrum was observed. The broadening and the shift of the binding energy of C_0 are attributed to the presence of the disordered borazine radicals and boron atoms atop the graphene film. A broadening of the C 1s peak and the appearance of new peaks at higher binding energies have been reported in [5] for hydrogen atoms adsorbed atop of Gr/Ir(111). However, in our experiment, no carbon components can be distinguished at higher energies. Based on this observation we conclude that a Gr film mainly covered by hydrogen atoms is an

Table 1: XPS peak parameters (in eV)

Surface	**Component**	**$E_{Binding}$ ±0.05**	**LFWHM**	**GFWHM ±0.05**
	N_0	-	-	-
1 ML Gr/Ir(111)	C_0 / C_1	284.31 / -	0.09*	0.80 / -
	B_0 / B_1	-	-	-
	N_0	397.92	0.10*	1.34
1 ML h-BN/Ir(111)	C_0 / C_1	-	-	-
	B_0 / B_1	190.18 / 188.53	0.52	0.90 / 0.26
1 ML Gr	N_0	-	-	-
+ 300 L Borazine	C_0 / C_1	284.23 / -	0.09*	0.78 / -
(no filament)	B_0 / B_1	-	-	-
1 ML Gr	N_0	398.31	0.10*	1.66
+ 300 L Borazine	C_0 / C_1	283.99 / 283.18	0.09*	1.06 / 1.58
with the filament	B_0 / B_1	190.12 / 188.23	0.52	1.94 / 1.40

**Tabulated values [28]*

unlikely scenario. Instead, we suggest that hydrogen atoms recombine and desorb as H_2 in the same way as with the catalyst-based CVD growth (see figure 11a), or remain bound to the borazine radicals. The C_1 component, centered at 283.18 eV, indicates that some of the carbon atoms are binding to another element, and its width (GFWHM of 1.58) suggests that the component includes several different types of C-atoms. From the analysis of the N 1s and B 1s spectra, we have concluded that both elements are interacting with carbon. Nitrogen and boron could be substituting carbon atoms in the graphene lattice, nevertheless this scenario is very unlikely since our experiment was performed at room temperature. Another and more likely explanation is that the C_1 component originates from the carbon atoms forming bonds with boron or nitrogen atoms atop. The interaction with boron and nitrogen combined with the change of bond length due to the re-hybridization to sp^3 of the carbon atom could explain the binding energy of 283.18 eV measured for the component C_1. Even though this explanation is more plausible, a complementary analysis of the coverage should be performed before assigning unequivocally the C_1 component.

In conclusion, we have demonstrated that the electron cracker generates reactive borazine radicals that attach to 1 ML graphene film. Our XPS characterization suggests a disordered structure of borazine radicals and atomic boron atop of the graphene layer. In the following sections, we will analyze the relative coverage of each element and the evolution of the whole system as a function of the temperature.

Coverage calibration

The intensity of each component can be used to calculate the relative coverage of each species on the surface. Nevertheless, the measured intensity depends not only on the coverage Θ_i. As expressed in equation 3.3, the intensity of the photoelectron peak of the element "i" is also proportional to the photoelectron total cross-section σ, the incoming photon flux, F, and the transmission function of the electron analyzer, T.

$$I_i \propto \Theta_i \cdot \sigma_i \cdot F \cdot T \tag{3.3}$$

The cross-section and the transmission function for the analyzer can be calculated or it is tabulated, but the photon flux is more difficult to obtain. This is because the number of photons that reaches the sample surface is affected by all the optical elements in the beamline. Every time that the photon energy is changed or the sample position is changed there is a risk that flux is changed. Moreover, it is common to have flux changes as function of time as the optical elements are heated by the intense radiation causing thermal expansion and beam drift which again results in flux changes at the sample position[18]. An alternative to calculating σ and T is to work with relative intensities. To do so we divide the area of the component "i" from the unknown surface (A) by the area of the peak measured on a known sample (B). Nevertheless, every time we change the photon energy to measure a spectrum, we will have a different incoming flux, so the dependence on F cannot be avoided by using relative coverages.

The intensity measured will also be affected if the surface analyzed is changed significantly. The addition of layers atop our initial surface will affect the mean free path of the photoelectrons, that now have to travel through different materials with different cross-sections to reach the vacuum (multilayer effects). In figure 18 we have shown the spectra of the C 1s and Ir $4d_{5/2}$ of 1 ML Gr/Ir(111) before and after dosing 300 L of borazine atop. It is clear that the intensity of both components is drastically reduced for the second measurement because of the change in the surface. Therefore the C 1s in spectrum A cannot be directly compared to C 1s in spectrum B. Diffraction effects will also affect the intensity measured. The photoelectron generated might scatter at the surface, resulting in different intensities depending on the measuring angle.

Because of these problems with absolute intensities, the best way to compare intensities obtained from different measurements is to normalize them to the intensity of the core-level from an element that will not change during the experiment. In our case, we used the iridium $4d_{5/2}$ peak. Furthermore, to minimize the changes of the incoming flux, both elements of interest should be measured with the same photon energy for every surface analyzed.

As an example, we can analyze the relative coverage of graphene after the dosing of 300 L of borazine on 1 ML Gr/Ir(111). The result obtained will help us clarify the interaction of

the boron and nitrogen with the graphene layer. We measured the Ir $4d_{5/2}$ and C 1s using a photon energy of 800 eV both for (a) the 1 ML of graphene reference surface and (b) the surface after the electron assisted dosing. The spectra measured are shown in figure 18. Each peak was fitted with a Voight function, and the area under each peak was obtained by numerical integration. We first calculated the relative area of the C 1s peak with respect to the Ir $4d_{5/2}$ peak. As sample (a) is a known surface (1 ML of Gr on Ir(111)), we can normalize the value obtained to 1 ML.

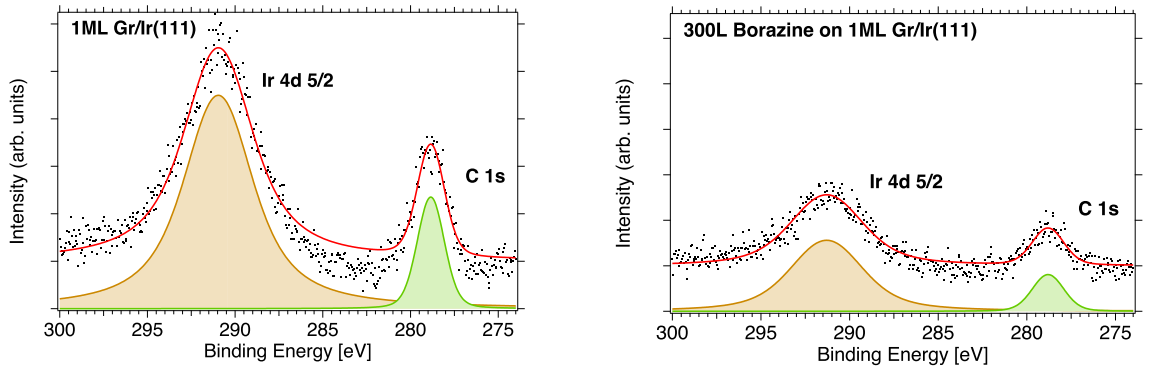

Figure 18: XPS measurements for coverage calibration of the core levels Ir($4d_{5/2}$) and C(1s) with an incident photon energy of 800 eV. a) Reference sample, 1 ML Gr/Ir(111). b) Same sample after dosing 300 L of borazine with the molecule cracker.

For the spectrum measured after dosing the borazine we follow the same procedure; first, we obtain the relative area of the C 1s peak with respect to the Ir $4d_{5/2}$ peak and then we convert the result obtained to monolayers by dividing by the intensity of the reference spectra. As it can be seen in table 2, the normalized intensity of the C 1s component is still equivalent to 1 ML after dosing borazine atop. This result confirms that the graphene layer is relatively intact, which means that the nitrogen and boron atoms did not substitute C atoms in the graphene lattice.

Table 2: Relative coverages

	Reference surfaces 1 ML Gr or 1 ML h-BN (coverage in ML ±0.25)	**1 ML Gr + 300 L borazine (coverage in ML ±0.25)**
C 1s	1	1.1
B 1s*	1	2.2
N 1s	1	1.2

**Includes both components of the B 1s spectra; B_0 and B_1.*

Previously in this master thesis, we concluded that the surface after the electron assisted growth was composed by borazine radicals and atomic boron atop of graphene. An important conclusion was also that a high amount of atomic boron was detected on the surface, while no atomic nitrogen appeared in the N 1s spectra. With the analysis of the relative coverages, we are able to understand the situation better. We calculated the relative intensities for all the components with respect to the Ir $4d_{5/2}$ peak using the method explained above and summarized the results in table 2. The inspection of this table shows that the reference values for a complete monolayer of h-BN are 1 ML nitrogen and 1 ML boron (1:1 B to N ratio)[8]. In contrast, by using the electron assisted growth technique, we obtained a 2:1 ratio of B:N, meaning that the relative coverage of the N 1s peak corresponds to a complete monolayer, while the relative intensity of the B 1s peak (including both components) corresponds to a coverage of two monolayers.

In the analysis of the B 1s spectrum after the electron assisted growth (see figure 17b) we noticed that the intensity ratio between the B_0 and B_1 components was 1:1, meaning that we measured the same amount of boron in borazine radicals than atomic boron. Knowing now that the total boron coverage is equivalent to 2 ML we can describe the surface as follows; half of the boron atoms (the component B_0) are part of the borazine radicals, forming a coverage equivalent a complete BN film together with the nitrogen (component N_0). The other half of boron (component B_1) is in the atomic form, covering the equivalent to 1 ML of the sample. We interpret this as the dissociation power of the filament is such, that atomic nitrogen and boron are produced when dosing borazine. Most likely, the nitrogen atoms diffuse on the graphene surface, form N_2 and desorb while the atomic boron remains adsorbed atop the graphene.

In figure 19 a sketch of the sample after dosing borazine with the molecule cracker is shown. From the complete analysis of the XPS measurements, we know that the graphene layer is intact underneath a disordered structure of borazine radicals and atomic boron. The C 1s spectrum also indicates that no hydrogen is adsorbed on the graphene. Most likely, the atomic hydrogen generated by the molecule cracker recombine to form H_2 and desorb from the surface. Nevertheless, it is not possible to determine if all the hydrogen is removed from the system. In figure 19 several possible scenarios for the borazine adsorbed on graphene are depicted (with and without hydrogen). In addition to the borazine radicals, we have found that with the molecule cracker we generate a significant amount of atomic boron that tends to remain adsorbed on the graphene. The borazine radicals also remain adsorbed on the graphene, most likely by forming N-C bonds. In contrast, the atomic nitrogen that is also likely to be generated by the electron beam could not be detected on the surface. Like hydrogen, it recombines to N_2 and desorbs from the surface.

[8] 1 ML is defined as the amount of B and N atoms in a complete BN film.

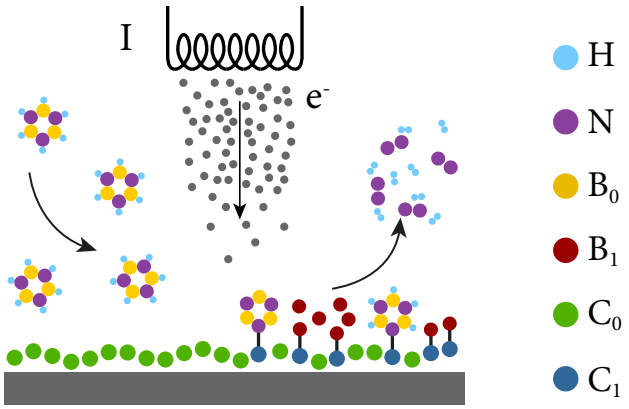

Figure 19: Schematic description of the resultant system after dosing of 300 L of borazine on 1 ML Gr/Ir(111) with the molecule cracker. The iridium substrate is represented as a grey block. Atop, the graphene layer with green balls representing the carbon atoms (component C_0 of the C 1s spectrum in figure 16). The blue balls in the graphene lattice represent carbon atoms re-hybridized to sp^3 and binding to nitrogen and boron (component C_1). The boron atoms are represented in yellow when part of the borazine radicals (B_0) or red when in atomic form (B_1). Finally, the nitrogen atoms (N_0) are represented as purple balls.

Besides the presence of atomic boron, we can conclude that the surface described corresponds to the first step of TPG growth presented in section 3.1. Therefore we have achieved the first step for growing a 2D crystal on an inert substrate.

3.2.2 Step 2: Temperature evolution

In the previous sections of this thesis, we have reviewed the growth techniques most commonly used for 2D materials on catalytic substrates. Then we have applied them for growing a complete monolayer of graphene and h-BN flakes on Ir(111). Finally, we have proven that we are capable of emulating the role of the catalytic substrate on 2D growth with a molecule cracker and tested its performance by dosing borazine atop inert graphene. The results obtained, represented schematically in figure 19, indicate that we have accomplished the first step of 2D crystal growth as we formed a disordered structure of radicals atop our substrate that is equivalent to the Ir(111) surface after dosing borazine at room temperature (see section 3.1.3).

In this section, we will report on our study of the temperature evolution of the system obtained via electron-assisted growth. The existent knowledge of TPG and CVD leads us to expect that, upon annealing, the borazine radicals will diffuse on the graphene and form the crystalline structure h-BN. Nevertheless, the change of substrate, the presence of atomic boron and its interaction with the graphene discussed in the previous section adds several degrees of complexity to our system.

We studied our sample with both STM and XPS techniques. To describe the growth of the 2D film we will first present the STM results that will provide a general overview of the surface and its evolution with the temperature. We will complement that information with a more detailed description provided by the analysis of the XPS measurements.

STM results

To understand how the different structures of our system evolve with the temperature, we have scanned the surface with a Scanning Tunneling Microscope (STM imaging) after stepwise annealing the surface. The temperature evolution of the surface for different annealing steps until the last temperature, 1273 K, is shown in panels b-h of figure 20.

Panel a shows an STM image of the pristine graphene film before the electron assisted growth. We can clearly see the characteristic moiré pattern and two different terraces of the iridium substrate underneath. In contrast, the second STM image shows an STM image of the same surface after the exposure to 300 L of borazine with the molecule cracker. Even though several iridium terraces are still visible (the step edges of those terraces have been highlighted in yellow in all images), it is clear that now the surface is covered with a disordered structure. As we dosed the same amount of borazine onto graphene and used same settings for the filament before this image was taken and before the XPS data discussed in the previous section was measured, we now can link this STM image to our XPS results. In other words, the image shown here gives the direct view of the disordered borazine radical structure described in the previous section and represented in figure 19.

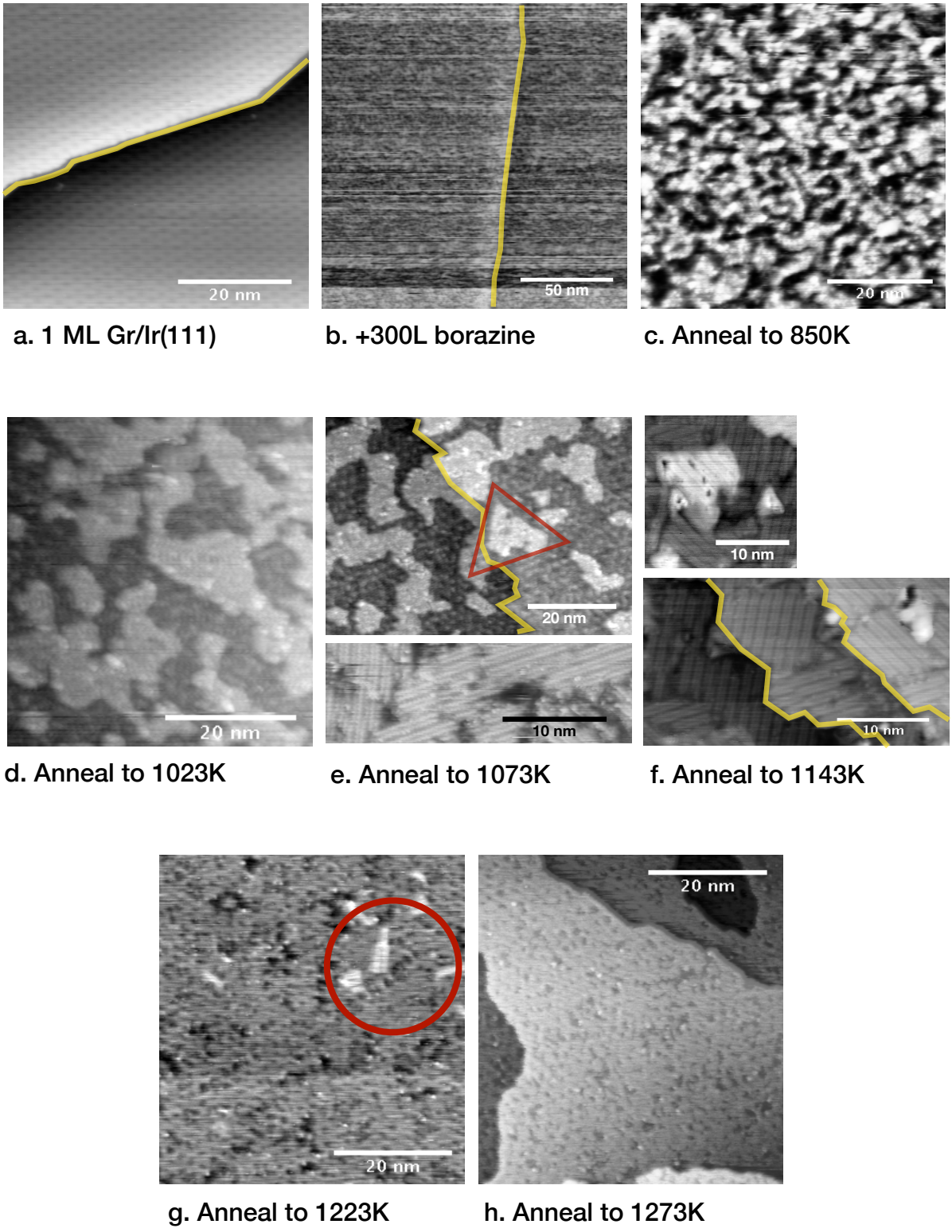

Figure 20: STM images of the evolution of 1 ML Gr/Ir(111) after the electron assisted dose of 300 L of borazine and its subsequent step-wise annealing. The iridium step edges are highlighted with yellow lines (images a, b, c, d and f) and characteristic BN structures are empathized with red triangles (images g and h). See main text for a detailed explanation of each image.

Panel c shows how the structure of the system changed after annealing to 850 K. We can see how the disordered structure has gained some order and starts forming a percolated network, similar to the structure observed by Farwick zum Hagen *et al.* [24] after dosing 2 L of borazine at room temperature for 30 s on iridium and annealing to 1000 K. In the next annealing step, panel d, bigger islands start forming and we begin to discern two different layers. Up to this temperature, the graphene film underneath has not been visible.

After annealing to 1073 K (figure 20, panel e), the islands become bigger and the characteristic triangular shape of the h-BN flakes can be recognized in some of the structures (example highlighted with a red triangle). It becomes more clear now that we have a multilayer structure, as two different levels can be clearly distinguished. In this same image, it is possible to observe a pattern in the lowest layer of the structure that resembles the graphene moiré. For this same annealing step, at certain STM image modes, we could observe the formation of chain-like structures (see panel e, bottom image).

The chain-like structures are also present after annealing to 1143 K (figure 20, image f). Now we can see that it covers the whole surface scanned, and distinguish three different orientations rotated 120° with respect to each other are observed. A similar structure was found on bare iridium by Valerius *et al.* [25] forming at the edges of the iridium terraces after bombarding the h-BN film grown atop with heavy ions. Petrović *et al.* reported the same results when analyzing the h-BN island growth on the same substrate [29]. Both articles describe the structures as boron nanoribbons forming a (6×2) superstructure on Ir(111) with three equivalent 120°-rotated variants. Because of the several studies reporting such structures to form on iridium, we are inclined to think that the ones visible in our STM images are indeed forming underneath the BN and Gr layers. See in figure 21 a high-resolution STM image of the surface where the atomic structure of the boron nanoribbons is clearly visible. In figure 21 b, an STM image of the boron nanoribbons reported by Valerius *et al.* in [25] has also been included as a reference.

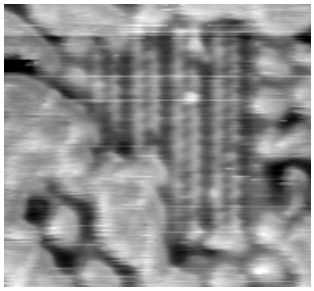

(a)

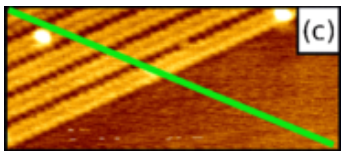

(b)

Figure 21: a) STM close-up of the boron nanoribbons and height profile over the blue line. The image was taken after dosing 300 L of borazine on 1 ML Gr/Ir(111) and annealing at 1223 K. b) Reference STM image reproduced from [25]: A bundle of boron stripes formed at the iridium surface after ion irradiating the h-BN structure grown atop and annealing at 1550 K.

After annealing at 1223 K, a dramatic change occurs. As we can see in panel g of figure 20, most of the nanoribbons are gone (the remaining ones have been highlighted with a red circle) and the surface left shows a clear, yet defective, moiré-like pattern. After annealing at 1273 K, there are no boron nanoribbons left at the sample (panel h in figure 20). It is clear that we have a multi-layer surface but those could be the substrate steps. The moiré patterns described before are still visible and still show the same defects.

If we consider the information presented so far, the temperature evolution of the surface can be summarized as follow:

Starting with the scenario presented in the previous section, we know that after dosing with the molecule cracker at room temperature we have a disordered structure of borazine radicals and atomic boron atop the graphene film. From the STM images presented, it becomes clear that the BN radicals diffuse around the surface and form islands that become larger upon annealing. Between 1023 K and 1073 K the graphene moiré pattern seems to become visible in the lowest layer, which could indicate that the BN layer is direct atop the graphene[9]. With increasing temperature, at approximately 1223K, the multilayer structure seems to lose layers and the moiré pattern becomes visible everywhere. This could be interpreted as the diffusion of the small islands towards the edges to form bigger flakes until the surface becomes a monolayer of BN atop graphene. Nevertheless, the interaction of this BN layer with the graphene cannot be deduced only from the STM images, we will need to analyze in detail the XPS data to better understand the system.

Taking a closer look at the atomic boron, the references found in the literature and the STM images suggest that boron diffuses underneath the graphene film upon annealing. As all graphene films, our film also contains defects and the boron atoms most likely diffuse underneath through these defects. The diffusion of atomic species under graphene (intercalation) has been widely studied and it is perfectly possible at the pressures and temperatures used for this experiment [30]. It is worth mentioning that only atomic boron seems to diffuse underneath graphene, which suggests that the Gr monolayer act as a filter for atomic species. From the images included in figure 20 we can see that at 1073 K the boron nanoribbons are already formed, which is a much lower temperature than the ones reported for the ribbon formation on iridium (1550 K in [25] and 1373 K in [29]). In [25] and [29] a high temperature was needed to dissociate the h-BN structures to generate the atomic boron. In our case, atomic boron was formed upon deposition by the electron assisted dissociation and less energy is therefore needed to form the nanoribbons.

The qualitative analysis of the STM images provides a first description of the temperature evolution of the system. To confirm and complement the interpretation of the STM images included in this section, XPS measurements were performed.

[9] As the lattice constant of h-BN and Gr is almost the same, it is possible that the h-BN film reflects the pattern of the graphene layer underneath.

XPS results

For the temperature dependent XPS experiments, we dosed a higher amount of borazine (600 L) onto graphene while operating the filament. A higher amount of borazine was used to increase the amount of boron and nitrogen deposited and, therefore, the intensity of their signal. Subsequently, we acquired N 1s, B 1s and C 1s spectra after stepwise annealing the surface, starting at room temperature until 1322 K at steps of 50 K. In figure 22 we can see the evolution of those core levels with temperature. In this section, we will first look at the boron and nitrogen spectra, where most of the change occurs. Afterward, we will complement the analysis with the information in the carbon measurements.

In the lowest boron spectra included in figure 22 we can see the same two components already discussed in section 3.2.1, B_0 and B_1. There we concluded that B_0 represented the boron within the borazine radicals and B_1 the atomic boron adsorbed on the graphene substrate. In the same figure, we can also notice that around 723 K a third component arises, B_2.

Before starting with the analysis of the binding energies of those three components and their evolution with the temperature, we will review first their relative intensities. Similar to what we did in section 3.2.1a, from the curve fit of each spectrum we obtained the relative intensity of each component. In this case, we calculated the area under each peak and normalized it to the area of the component B_0 at room temperature. With this approach, we can see how the intensity of each component evolves with the temperature. The results can be seen in figure 23a. There it becomes clear that the intensity of the component B_0 (yellow area) is maintained relatively constant for all the annealing steps. This suggests that the BN coverage is constant. In contrast, the intensity of component B_1 (red area) starts decreasing at 600 K and it is almost zero at the highest annealing step, 1323 K. This reveals that the atomic boron is somehow being removed from the surface. Based on the STM images presented earlier in this text, a plausible explanation is that the atomic boron diffuses underneath the graphene layer. At the same temperature that the B_1 component starts decreasing, the intensity of the new component B_2 starts increasing (orange area in figure 23a). Therefore, we assign this new component to the boron intercalated under graphene. At high temperatures, the intensity of both B_1 and B_2 are almost zero, meaning that, after annealing at 1323 K, we obtained a surface covered mainly by a BN film. The analysis of the binding energies will provide more information about the nature of such structure.

Starting with the component B_0, in figures 22 and 23b we can see that it evolves towards higher binding energies upon annealing. The binding energy measured at room temperature (189.9 eV bottom spectra in figure 22) is equivalent to the one measured after dosing 300 L of borazine on 1 ML graphene (190.12 eV, result already presented in section 3.2.1). Upon annealing, between 800 K and 1000 K, the binding energy shifts to a maximum value of 190.48 eV, which correspond to the shift reported by Orlando *et al.* when studying the

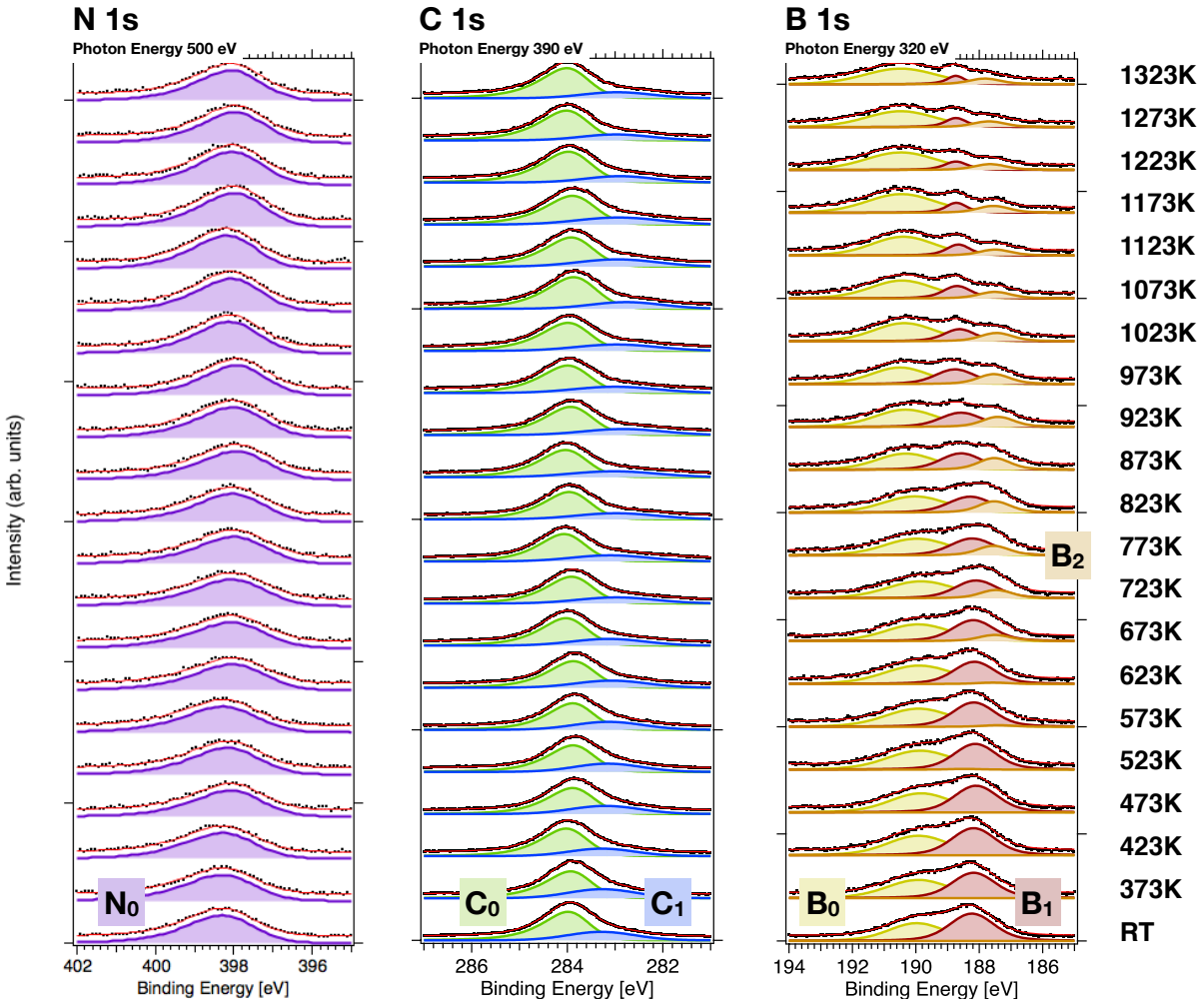

Figure 22: XPS measurements of 1 ML graphene after dosing 600 L of borazine with the molecule cracker on. The evolution with the temperature of the spectra N 1s (left), C 1s (middle) and B 1s (right) is shown. The bottom spectra correspond to the measurement at RT and the top one to the measurement after annealing to 1322 K. The annealing steps are of 50 K. The components used to fit the experimental data have been included (purple for nitrogen, Green, and Blue for carbon and Yellow, Red and Orange for boron). See main text for the interpretation of the data.

epitaxial growth of h-BN on Ir(111) [26] (from 189.7 eV for molecular borazine to 190.5 eV for h-BN). Therefore, we can deduce that a crystalline structure similar to h-BN starts forming on our sample at 800 K.

At the same temperature that the BN layer starts crystallizing, the B_1 component also starts shifting to higher binding energies (from 188.3 eV to 188.74 eV). Further annealing does not change the binding energy more. The change can be clearly seen in figures 22 and 23b. The main idea behind the analysis of the B 1s spectra is that the B_0 and B_1 components are linked and shift to higher energies by the same amount, this means that

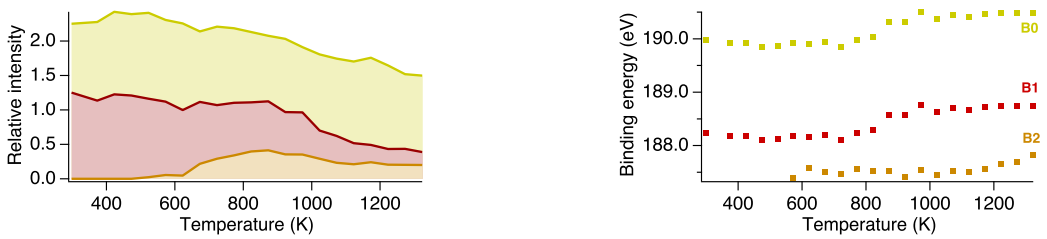

Figure 23: Temperature evolution of the three B 1s components, B_0 (yellow), B_1 (red), and B_2 (orange) a) Relative intensity. b) Binding energy. See main text for a detailed explanation.

a change in the surface is affecting both components in the same way. With the analysis of the relative intensities we have already seen that the component B_2 appears at 600 K, right before B_0 and B_1 start shifting in binding energy. Therefore we can link both shifts to the removal of atomic boron from atop the graphene layer. The reduction of atomic boron facilitates the formation of the BN crystalline structure and, at the same time, the remaining boron adsorbed atop graphene will experience a change in binding energy because of the overall change in the surface structure.

The binding energy of the last component on the B 1s spectra, B_2, is constant during almost all the different annealing steps, centered at 187.5 eV. Only for temperatures higher than 1173 K it slightly increases until reaching 187.83 eV (see figures 22 and 23b). Some of the reported values from atomic boron are; 188.9 eV for atomic boron trapped underneath h-BN flakes [25], 188.6 eV for atomic boron on iridium [26], and 188-188.5 eV for boron either on the surface or penetrating in the iridium surface [27]. The initial energy of the B_2 component (187.5 eV) corresponds to lower range of those values, nevertheless, based on our previous analysis of the rest of the B 1s components, we assign B_2 to the atomic boron trapped underneath the graphene. The shift towards higher binding energies (up to 187.83 eV) is interpreted as the atomic boron diffusing into the iridium substrate. Both statements are in agreement with the binding energies reported in [27] and the STM images presented earlier in this section, where no boron structures could be distinguished in our sample after annealing at 1273 K. From the analysis of this component we can conclude that atomic boron intercalates under graphene for temperatures higher than 600 K, and that, after annealing at 1273 K the boron diffuses into the iridium substrate. However, no sign on the XP spectra supports the conclusion made with the analysis of STM images that, at 1073 K boron nanoribbons are formed underneath graphene. We interpret that the change in binding energy upon the formation of such structures is too weak to be distinguished with the experimental setup used.

Continuing our analysis with the nitrogen measurements, we can see in figure 22 that the intensity of the nitrogen component is maintained constant for all the annealing steps. This observation, together with the analysis of the B_0, corroborate the assumption that the

surface is always covered by a nitrogen-based film, probably BN, and that no significant desorption of nitrogen occurs upon annealing.

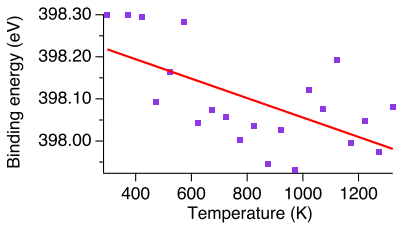

Figure 24: Evolution of the N 1s peak with the temperature. Starting with its maximum value of 398.3 eV at RT, it reaches a minima of 397.95 eV at 973 K and ends at 398.08 eV at 1323 K.

The analysis of the binding energy of N 1s also confirms the formation of a crystalline structure between 800 K and 1000 K. The binding energy measured at the lowest spectra (398.3 eV) is identical to the value measured after dosing 300 L of borazine with the filament in section 3.2.1 (398.31 eV). There we concluded that the N 1s component after electron assisted growth represented nitrogen atoms in a disordered structure of borazine radicals binding to the graphene layer below. With the increasing temperature we observe a shift of the binding energy towards lower values (from 398.3 eV to 397.9 eV, see figures 22 and 24). This shift corresponds to the one reported by [27] for the formation of an ordered h-BN structure (from 397.7 eV to 397 eV). The overall difference between the values in [27] and the values obtained in our experiment is due to the interaction with the substrate (the binding of the nitrogen atoms to the iridium will be different to the binding to an inert substrate such as graphene), nevertheless, the shift due to the h-BN formation is the same.

The temperature at which BN starts crystallising on graphene is considerably lower than the one used for h-BN growth on Ir(111) (1140 K, see section 3.1.3) and than the temperatures previously reported in [24, 27, 26] (1270 K, 950 K, and 1170 K respectively). A lower formation temperature also indicates a weak interaction between the borazine radicals and the graphene layer, which means that it costs less energy (i.e. temperature) to induce mobility and start to form the crystalline structure.

Finally, we analyze the temperature evolution of the carbon spectra. In figure 22, we observe that the components obtained after dosing 600 L of borazine on 1 ML graphene (C_0 centered at 283.98 eV and C_1 at 283.29 eV) are equivalent to the ones measured for 300 L of borazine (283.99 and 283.18 eV respectively, see section 3.2.1). These components were already assigned to carbon in the graphene lattice and carbon with nitrogen or boron adsorbed atop respectively. In figure 25a is clearly visible that both components are present for all the annealing steps, and their relative intensity is maintained constant[10]. The constant intensity of C_0 indicates that the graphene coverage is preserved. In addition, the

[10]We calculated the area under each component and normalized it to the area of C_0 at RT.

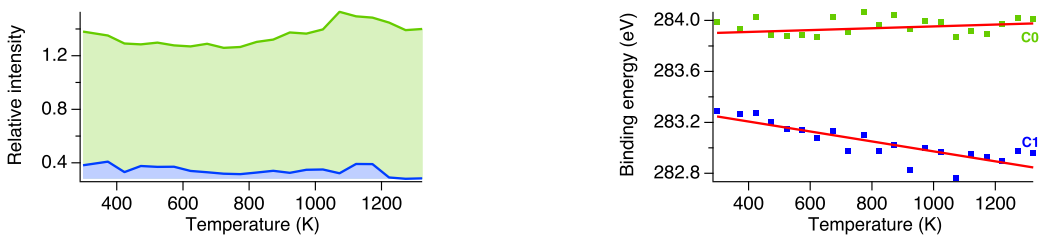

Figure 25: Temperature evolution of the two C 1s components, C_0 (green) and C_1 (blue) a) Relative intensity. b)Binding energy evolution. C_0 is constant around the value 283.9 eV for all the annealing steps. C_1, on the other hand, constantly shifts to lower binding energies, from 283.29 eV at RT to 282.96 eV at the highest annealing step, 1173 K. See main text for an interpretation of the data.

constant intensity of the component C_1 suggests a constant coverage of adsorbates on the graphene layer for all the different annealing temperatures.

The binding energy for the C_0 component remains constant for all the temperatures (figure 25b). In addition, the width of the peak is also invariable with the increasing temperature[11]. None of those indicate that the boron atoms intercalate under the graphene layer. We interpret that, because of the presence of BN structures atop, any weak changes on the C_0 component (such as intercalation signs) will be difficult to observe. Therefore, from the analysis of the carbon spectra, we can not confirm the temperature at which the boron atoms intercalate under graphene.

The second component of the carbon spectrum, C_1, gives us a bit more information. After annealing the sample, we observe a general trend to lower binding energies (from 283.29 eV at RT to 282.96 at 1173 K, see figure 25b). At the same time, the width of the peak increases from 1.6 (GFWHM) to ∼2 at 873 K and then decreases again until reaching 1.68 at 1323 K. The slight shift in binding energy could be interpreted as a change in the bond with the boron atoms, which is corroborated by the change in width. One plausible explanation is that the boron atoms adsorbed on the graphene start binding to the nitrogen atop, which would increase the C-B bond length and, therefore, reduce the C 1s binding energy. Nevertheless this assumption cannot be confirmed by any changes in the boron spectra.

To summarize, although some of the details about our surface cannot be elucidated by either XPS or STM, the joint analysis of both types of measurements allowed us to obtain a fairly complete picture of our system and we are able to affirm that we have grown a BN/Gr heterostructure. In the following section, we will use all the information obtained to present a model that describes the main steps for electron assisted growth of BN on 1 ML of graphene.

[11]The GFWHM oscillates between 1.1 and 1.2, the exact values can be found in table 4, appendix A

4 Conclusions

We have now proven the functionality of the electron assisted growth technique. First, we showed that, without the dissociating function of the molecule cracker, it is not possible to deposit the precursor molecule on a substrate that is not catalytically active. Then we performed the same experiment with the molecule cracker on and deposited borazine radicals onto the same inert substrate, 1 ML graphene. Finally, we analyzed the temperature evolution of the system. Our results indicate that with the electron assisted growth technique, we have succeeded in growing a BN/Gr heterostructure atop the Ir(111) substrate. The growth process can be described by the following main four steps, represented schematically in figure 26:

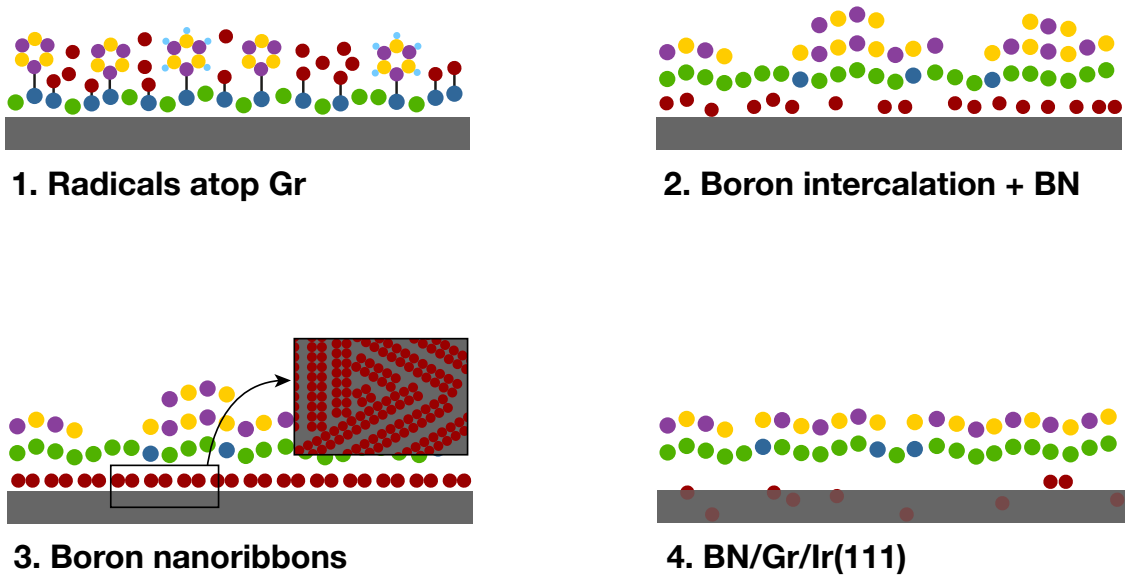

Figure 26: Schematic description of the model proposed for the h-BN/Gr heterostructure grown on Ir(111) via electron assisted growth. The grey block represents the iridium substrate. Green and blue balls represent the carbon atoms (without and with adsorbates atop respectively). Red balls represent atomic boron. Boron binding to graphene is represented by orange balls. Finally, yellow and purple balls represent boron and nitrogen atoms in borazine radicals. See the main text for a detailed explanation of each step.

1. Disordered radicals atop graphene

Starting with the surface obtained right after the room temperature borazine dosing with the filament on, the STM images revealed that a disordered BN structure formed on our sample. The analysis of the corresponding XP spectra showed that the disordered structure was formed by atomic boron (1 ML) and borazine radicals (1 ML). In addition, we showed that the graphene layer remains intact after the borazine dosing, and that the borazine radicals and atomic boron were adsorbed on the graphene layer by forming N-C and B-C bonds, respectively.

2. Diffusion of atomic boron under graphene and crystallization of BN
The analysis of the B 1s spectra showed that around 600 K the atomic boron starts to diffuse underneath the graphene layer. At the same temperature, and due to the change in the B to N ratio atop the graphene, the BN crystalline structure started to form. This is a noticeable result, as the graphene layer here acts as a filter that allows atomic species to pass, while large molecules are trapped above the film. As the atomic B atoms are filtered away from the graphene surface the formation of the 2D BN films starts. The complementary analysis of the N 1s spectra showed that the BN film developed between 773 K and 1000 K. In the STM images, we observed that the BN crystalline structures started to form as flakes atop each other, but with the increasing temperature the smaller islands diffused to the edges of the bigger ones and a single layer of BN is obtained.

3. Formation of B nanoribbons
STM images revealed that at 1073 K the atomic boron underneath graphene re-ordered in boron nanoribbons forming what it seems to be a (6×2) superstructure on Ir(111) with three equivalent 120°-rotated domains. In this case, the formation of such structures could not be corroborated by the XPS measurements.

4. Diffusion of B into iridium substrate and final structure
After annealing at temperatures higher than 1173 K both the STM and XPS measurements indicated that the atomic boron at the interphase between graphene and the Ir(111) surface diffused into the bulk of the single crystal surface. The remaining surface was then composed by 1 ML Gr covered by a BN crystalline film. The STM images showed that the BN structure grown atop graphene was not perfect and some defects or holes were present.

To conclude, we have proven the functionality of the electron assisted growth technique as a powerful and simple tool for growing single layers of 2D materials on an inert substrate.

5 Outlook

In previous sections, we have proven the functionality of the molecule cracker as a substitute for the catalytic substrate in 2D materials growth. The interplay of STM and XPS was used to give a fairly complete picture of the surface obtained with the electron assisted growth technique. Nevertheless, key aspects of the BN/Gr heterostructure, such as the temperature evolution of the absolute coverage, the structure of the BN layer, and the interaction between the Gr/BN layers, could not be determined.

In order to obtain a complete description of the BN/Gr heterostructure, further experiments need to be done. First, an additional STM characterization of the BN/Gr heterostructure should be performed. By obtaining atomically resolved images of the top BN layer we expect to be able to determine its structure and orientation with respect to the graphene below. These are very relevant aspects of the 2D layer that will affect the properties of the BN/Gr heterostructure [31]. Combined with the STM images, a LEED (Low-Energy Electron Diffraction) study of the temperature evolution of the system would be interesting. With LEED we would be able to follow the development of the crystalline structure as it develops upon annealing. Another interesting approach would be characterizing the formation of BN/Gr with Low-Energy Electron Microscopy (LEEM) combined with Low-Energy Electron Reflectivity (LEER). LEEM will provide a more general overview of the different structures forming in our sample. With the same experimental setup, we can obtain diffraction and reflection patterns from different points of interest. Therefore, with LEEM we should be able to monitor the evolution of specific crystalline structures forming in the surface and co-existing phases will be easy to identify. In addition, the reflectivity spectra can be used to determine the thickness of those structures [22]. This experimental approach could be relevant during the formation of the BN structure where a multi-layered BN film seems to develop. Finally, a high-resolution XPS study should be addressed. The low energy resolution of the electron analyzer, combined with the low intensity of the beam at high photon energies made impossible to discern relevant features on the spectra. Future XPS characterization of the BN/Gr heterostructure in a High-resolution-XPS beamline such as the SuperESCA beamline of ELETTRA Synchrotron or at the future FlexPES beamline at MAX IV would be the next step for understanding better this 2D stacked heterostructure.

Despite the limitations presented above, the results obtained in this first study of electron assisted growth constitutes a promising start for the further development of the technique. First of all, the simplicity of the setup presented enables its immediate implementation in 2D materials growth research. For example, preliminary results not included in this thesis showed that with this method it is also possible to grow the opposite structure: graphene on an h-BN substrate. In addition, with electron assisted growth we have obtained a pure 2D heterostructure of BN and Gr which, to our knowledge have not been achieved before by direct growth. Until now, research on stacked heterostructures has been focused on growing the 2D layer on a thin film on the desired substrate [10]. Our technique opens the

door to growing multi-layer heterostructures of alternating 2D materials on any substrate. For example, one could form a stacked h-BN/Gr/h-BN film. This specific heterostructure is especially interesting because it has been shown that, encapsulating the graphene layer between h-BN, leads to an improved stability of the Gr layer to ambient exposure [32]. The direct fabrication of a graphene-based device that is stable at ambient pressures would be of great interest.

Another interesting conclusion of our results is that the 2D crystal grown on graphene forms at a lower temperature than in other substrates. This opens the possibility of using the electron assisted growth setup to grow crystalline layers atop substrates that can not withstand high temperatures. Applying this technique to grow 2D materials on the typical substrate used for device characterization, Si or SiO_2, would be a really interesting next step in electron assisted growth research. Depending on the results obtained, it could enable direct characterization of the electronic properties of 2D stacked heterostructures, as no transfer to another substrate would be necessary. In addition, applying this technique to very inert surfaces such as Au(111) or Ag(111) would constitute another interesting next step for the continuation of the research with electron assisted growth.

Finally, the molecule cracker could be used as a simple way to generate radicals from a molecular gas. For example, the cracker could be used for functionalizing graphene or other 2D materials by adsorbing the produced radicals atop. A potential improvement of the setup could be to implement an additional mass-selector device, for example, a Wien filter. The resulting setup could then be used in studies of molecule adsorption and functionalization of 2D layers.

By all the above we conclude that the Electron assisted growth technique presented in this work conform a very promising tool for further research in 2D materials growth and functionalization.

References

[1] A. K. Geim and K. S. Novoselov. The rise of graphene. *Nature Materials*, 6:183 EP –, 03 2007.

[2] K. S. Novoselov, A. K. Geim, S. V. Morozov, D. Jiang, Y. Zhang, S. V. Dubonos, I. V. Grigorieva, and A. A. Firsov. Electric field effect in atomically thin carbon films. *Science*, 306(5696):666–669, 2004.

[3] Sumio Iijima. Helical microtubules of graphitic carbon. *Nature*, 354:56 EP –, 11 1991.

[4] H. W. Kroto, J. R. Heath, S. C. O'Brien, R. F. Curl, and R. E. Smalley. C60: Buckminsterfullerene. *Nature*, 318:162 EP –, 11 1985.

[5] Jakob Holm Jørgensen, Antonija Grubišić Čabo, Richard Balog, Line Kyhl, Michael N. Groves, Andrew Martin Cassidy, Albert Bruix, Marco Bianchi, Maciej Dendzik, Mohammad Alif Arman, Lutz Lammich, José Ignacio Pascual, Jan Knudsen, Bjørk Hammer, Philip Hofmann, and Liv Hornekaer. Symmetry-driven band gap engineering in hydrogen functionalized graphene. *ACS Nano*, 10(12):10798–10807, 2016. PMID: 28024374.

[6] Qiang Fu and Xinhe Bao. Surface chemistry and catalysis confined under two-dimensional materials. *Chem. Soc. Rev.*, 46:1842–1874, 2017.

[7] Haolin Wang, Yajuan Zhao, Yong Xie, Xiaohua Ma, and Xingwang Zhang. Recent progress in synthesis of two-dimensional hexagonal boron nitride. *Journal of Semiconductors*, 38(3):031003, 2017.

[8] Gianluca Giovannetti, Petr A. Khomyakov, Geert Brocks, Paul J. Kelly, and Jeroen van den Brink. Substrate-induced band gap in graphene on hexagonal boron nitride: Ab initio density functional calculations. *Phys. Rev. B*, 76:073103, Aug 2007.

[9] C. R. Dean, A. F. Young, I. Meric, C. Lee, L. Wang, S. Sorgenfrei, K. Watanabe, T. Taniguchi, P. Kim, K. L. Shepard, and J. Hone. Boron nitride substrates for high-quality graphene electronics. *Nature Nanotechnology*, 5:722 EP –, 08 2010.

[10] Wei Yang, Guorui Chen, Zhiwen Shi, Cheng-Cheng Liu, Lianchang Zhang, Guibai Xie, Meng Cheng, Duoming Wang, Rong Yang, Dongxia Shi, Kenji Watanabe, Takashi Taniguchi, Yugui Yao, Yuanbo Zhang, and Guangyu Zhang. Epitaxial growth of single-domain graphene on hexagonal boron nitride. *Nature Materials*, 12:792 EP –, 07 2013.

[11] Harald Ibach. Physics of surfaces and interfaces. *Springer-Verlag Berlin Heidelberg*, 2006.

[12] G. Binnig, H. Rohrer, Ch. Gerber, and E. Weibel. Surface studies by scanning tunneling microscopy. *Phys. Rev. Lett.*, 49:57–61, Jul 1982.

[13] P. Sutter. Science of microscopy - scanning tunneling microscopy in surface science. *Springer*, 2007.

[14] Kai M. Siegbahn. Electron spectroscopy for atoms, molecules and condensed matter. In *Nobel Lecture*, 1981.

[15] Gwyn P. Williams. X-ray data booklet section 1.1 electron binding energies x-ray data booklet section 1.1 electron binding energies x-ray data booklet. section 1.1 electron binding energies. Lawrence Berkeley National Laboratory, October 2009.

[16] Jan Knudsen, Peter J. Feibelman, Timm Gerber, Elin Grånäs, Karina Schulte, Patrick Stratmann, Jesper N. Andersen, and Thomas Michely. Clusters binding to the graphene moiré on ir(111): X-ray photoemission compared to density functional calculations. *Phys. Rev. B*, 85:035407, Jan 2012.

[17] A. Zangwill. Physics at surfaces. *Cambridge University Press, Cambridge*, 1988.

[18] C.S. Fadley. X-ray photoelectron spectroscopy: Progress and perspectives. *Journal of Electron Spectroscopy and Related Phenomena*, 178-179:2 – 32, 2010. Trends in X-ray Photoelectron Spectroscopy of solids (theory, techniques and applications).

[19] Søren Pape Møller Niels Hertel and Jørgen S. Nielsen. *ASTRID2 – the UV and soft x-ray synchrotron light source with the ultimate brilliance*. Department of Physics and Astronomy Aarhus University, Ny Munkegade 120, Building 1520 DK 8000 Arhus C Denmark, July 2009.

[20] Zheshen Li. www.isa.au.dk/facilities/astrid2/beamlines/au-matline/au-matline.asp, accessed 1st may 2018, last modified 29 september 2017.

[21] Louis Nilsson, Mie Andersen, Richard Balog, Erik Lægsgaard, Philip Hofmann, Flemming Besenbacher, Bjørk Hammer, Ivan Stensgaard, and Liv Hornekær. Graphene coatings: Probing the limits of the one atom thick protection layer. *ACS Nano*, 6(11):10258–10266, 2012. PMID: 23106828.

[22] Devashish P. Gopalan, Patrick C. Mende, Sergio C. de la Barrera, Shonali Dhingra, Jun Li, Kehao Zhang, Nicholas A. Simonson, Joshua A. Robinson, Ning Lu, Qingxiao Wang, and et al. Formation of hexagonal boron nitride on graphene-covered copper surfaces. *Journal of Materials Research*, 31(7):945–958, 2016.

[23] Elin Grånäs. Above and below graphene: Nanoparticle chemistry and interface reactions. *Lund University*, 2014.

[24] Ferdinand H. Farwick zum Hagen, Domenik M. Zimmermann, Caio C. Silva, Christoph Schlueter, Nicolae Atodiresei, Wouter Jolie, Antonio J. Martínez-Galera, Daniela Dombrowski, Ulrike A. Schröder, Moritz Will, Predrag Lazić, Vasile Caciuc, Stefan Blügel, Tien-Lin Lee, Thomas Michely, and Carsten Busse. Structure and growth of

hexagonal boron nitride on ir(111). *ACS Nano*, 10(12):11012–11026, 2016. PMID: 28024332.

[25] Philipp Valerius, Charlotte Herbig, Moritz Will, Mohammad A. Arman, Jan Knudsen, Vasile Caciuc, Nicolae Atodiresei, and Thomas Michely. Annealing of ion-irradiated hexagonal boron nitride on ir(111). *Phys. Rev. B*, 96:235410, Dec 2017.

[26] Fabrizio Orlando, Rosanna Larciprete, Paolo Lacovig, Ilan Boscarato, Alessandro Baraldi, and Silvano Lizzit. Epitaxial growth of hexagonal boron nitride on ir(111). *The Journal of Physical Chemistry C*, 116(1):157–164, 01 2012.

[27] D. Usachov, A. Fedorov, O. Vilkov, V. K. Adamchuk, L. V. Yashina, L. Bondarenko, A. A. Saranin, A. Grüneis, and D. V. Vyalikh. Experimental and computational insight into the properties of the lattice-mismatched structures: Monolayers of h-bn and graphene on ir(111). *Phys. Rev. B*, 86:155151, Oct 2012.

[28] J.L. CAMPBELL and TIBOR PAPP. Widths of the atomic k–n7 levels. *Atomic Data and Nuclear Data Tables*, 77(1):1 – 56, 2001.

[29] Marin Petrović, Ulrich Hagemann, Michael Horn von Hoegen, and Frank-J. Meyer zu Heringdorf. Microanalysis of single-layer hexagonal boron nitride islands on ir(111). *Applied Surface Science*, 420:504 – 510, 2017.

[30] Ulrike A Schröder, Marin Petrović, Timm Gerber, Antonio J Martínez-Galera, Elin Grånäs, Mohammad A Arman, Charlotte Herbig, Joachim Schnadt, Marko Kralj, Jan Knudsen, and Thomas Michely. Core level shifts of intercalated graphene. *2D Materials*, 4(1):015013, 2017.

[31] K. S. Novoselov, A. Mishchenko, A. Carvalho, and A. H. Castro Neto. 2d materials and van der waals heterostructures. *Science*, 353(6298), 2016.

[32] Viktoryia Shautsova, Adam M. Gilbertson, Nicola C. G. Black, Stefan A. Maier, and Lesley F. Cohen. Hexagonal boron nitride assisted transfer and encapsulation of large area cvd graphene. *Scientific Reports*, 6:30210 EP –, 07 2016.

Appendices

A Parameters for XPS fitting

Table 3: Fitting Parameters for N 1s spectra.

Temp. ±10 (K)	**$E_{Binding}$ ±0.05 (eV)**	**GFWHM ±0.04 (eV)**	**Relative area**
298	398.30	1.80	1.0
373	398.30	1.88	1.0
423	398.29	1.86	1.0
473	398.09	1.83	1.0
523	398.17	1.82	1.0
573	398.28	1.91	1.0
623	398.04	1.91	1.0
673	398.07	1.94	1.0
723	398.06	1.95	1.0
773	398.00	1.88	1.0
823	398.04	1.83	1.0
873	397.95	1.84	1.1
923	398.03	1.82	1.1
973	397.93	1.70	1.0
1023	398.12	1.72	1.1
1073	398.08	1.73	1.1
1123	398.19	1.73	1.2
1173	397.99	1.73	1.2
1223	398.05	1.74	1.2
1273	397.97	1.69	1.0
1323	398.08	1.74	1.1

LFWHF = 0.1 eV. Tabulated value from [28]

Table 4: Fitting Parameters for C 1s spectra, component C_0.

Temp. ±10 (K)	**$E_{Binding}$ ±0.02 (eV)**	**GFWHM ±0.02 (eV)**	**Relative area**
298	283.98	0.97	1.0
373	283.93	0.97	0.9
423	284.02	0.99	1.0
473	283.89	1.00	0.9
523	283.88	0.99	0.9
573	283.89	0.97	0.9
623	283.87	0.99	0.9
673	284.03	0.98	1.0
723	283.91	1.00	0.9
773	284.07	0.99	1.0
823	283.96	1.00	1.0
873	284.04	1.03	1.0
923	283.93	1.04	1.0
973	283.99	1.05	1.0
1023	283.99	1.04	1.0
1073	283.87	1.07	1.2
1123	283.92	1.04	1.1
1173	283.89	1.07	1.1
1223	283.98	1.07	1.2
1273	284.02	1.04	1.1
1323	284.01	1.02	1.1

LFWHF = 0.09 eV. Tabulated value from [28]

Table 5: Fitting Parameters for C 1s spectra, component C_1.

Temp. ±10 (K)	**$E_{Binding}$ ±0.02 (eV)**	**GFWHM ±0.06 (eV)**	**Relative area**
298	283.29	1.60	0.4
373	283.27	1.62	0.4
423	283.28	1.58	0.3
473	283.20	1.66	0.4
523	283.15	1.60	0.4
573	283.14	1.66	0.4
623	283.08	1.72	0.3
673	283.14	1.77	0.3
723	282.97	1.88	0.3
773	283.10	1.86	0.3
823	282.97	1.95	0.3
873	283.03	2.09	0.3
923	282.83	1.94	0.3
973	283.00	2.01	0.3
1023	282.97	1.98	0.3
1073	282.77	1.73	0.3
1123	282.95	1.93	0.4
1173	282.93	1.99	0.4
1223	282.90	1.65	0.3
1273	282.97	1.70	0.3
1323	282.96	1.68	0.3

LFWHF = 0.09 eV. Tabulated value from [28]

Table 6: Fitting Parameters for B 1s spectra, component B_0.

Temp. ±10 (K)	**$E_{Binding}$ ±0.05 (eV)**	**GFWHM ±0.08 (eV)**	**Relative area**
298	189.98	1.79	1.0
373	189.92	2.06	1.1
423	189.92	2.00	1.2
473	189.84	2.02	1.2
523	189.87	2.19	1.2
573	189.92	2.17	1.2
623	189.90	2.30	1.3
673	189.93	2.12	1.1
723	189.84	2.24	1.1
773	189.97	2.13	1.1
823	190.03	2.06	1.0
873	190.32	1.89	1.0
923	190.32	2.00	1.1
973	190.51	1.82	0.9
1023	190.37	1.98	1.1
1073	190.44	2.05	1.1
1123	190.40	2.06	1.2
1173	190.46	2.27	1.3
1223	190.48	2.33	1.2
1273	190.48	2.29	1.1
1323	190.48	2.40	1.1

LFWHF = 0.52 eV. Obtained from the fit of B 1s spectrum at RT.

Table 7: Fitting Parameters for B 1s spectra, component B_1.

Temp. ±10 (K)	**$E_{Binding}$ ±0.05 (eV)**	**GFWHM ±0.06 (eV)**	**Relative area**
298	188.23	1.35	1.3
373	188.18	1.31	1.1
423	188.18	1.33	1.2
473	188.10	1.33	1.2
523	188.13	1.29	1.1
573	188.18	1.27	1.1
623	188.16	1.23	1.0
673	188.19	1.23	0.9
723	188.10	1.27	0.8
773	188.23	1.32	0.8
823	188.29	1.31	0.7
873	188.58	1.24	0.7
923	188.58	1.24	0.6
973	188.76	1.17	0.6
1023	188.63	0.84	0.4
1073	188.70	0.74	0.4
1123	188.66	0.56	0.3
1173	188.72	0.44	0.3
1223	188.74	0.54	0.2
1273	188.74	0.46	0.2
1323	188.74	0.30	0.2

LFWHF = 0.52 eV. Obtained from the fit of B 1s spectrum at RT.

Table 8: Fitting Parameters for B 1s spectra, component $B_1 2$.

Temp. ±10 (K)	**$E_{Binding}$ ±0.05 (eV)**	**GFWHM* (eV)**	**Relative area**
298	-	-	0.0
373	-	-	0.0
423	-	-	0.0
473	-	-	0.0
523	-	-	0.0
573	187.40	0.90	0.1
623	187.57	0.90	0.0
673	187.51	0.90	0.2
723	187.47	0.90	0.3
773	187.56	0.90	0.3
823	187.52	0.90	0.4
873	187.53	0.90	0.4
923	187.41	0.90	0.4
973	187.54	0.90	0.4
1023	187.46	0.90	0.3
1073	187.51	0.90	0.2
1123	187.50	0.90	0.2
1173	187.56	0.90	0.2
1223	187.66	0.90	0.2
1273	187.69	0.90	0.2
1323	187.83	0.90	0.2

*$LFWHF = 0.52\,eV$. Obtained from the fit of B 1s spectrum at RT. *fixed value for the fit to converge.*

B Additional STM images

In this appendix we included additional STM images obtained from the BN/Gr heterostructure during the different annealing steps.

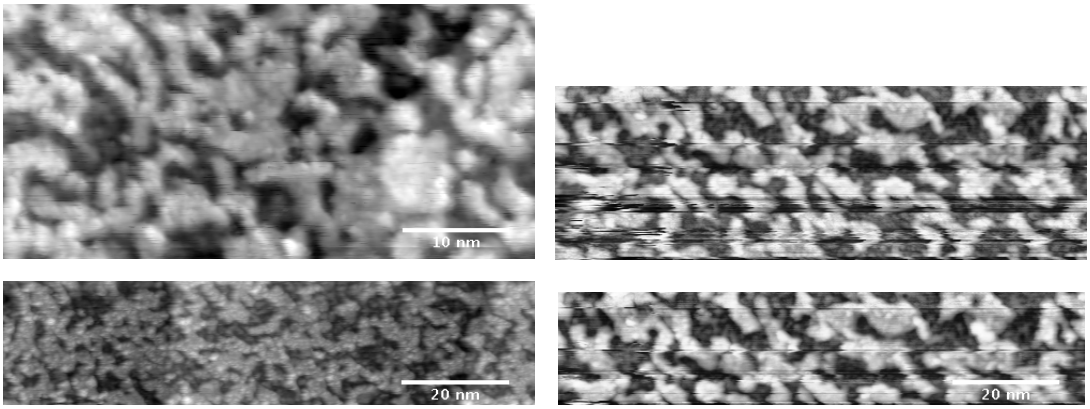

Figure 27: STM images from the Gr/Ir(111) surface after dosing 300 L of borazine with the molecule cracker and annealing at 903 K.

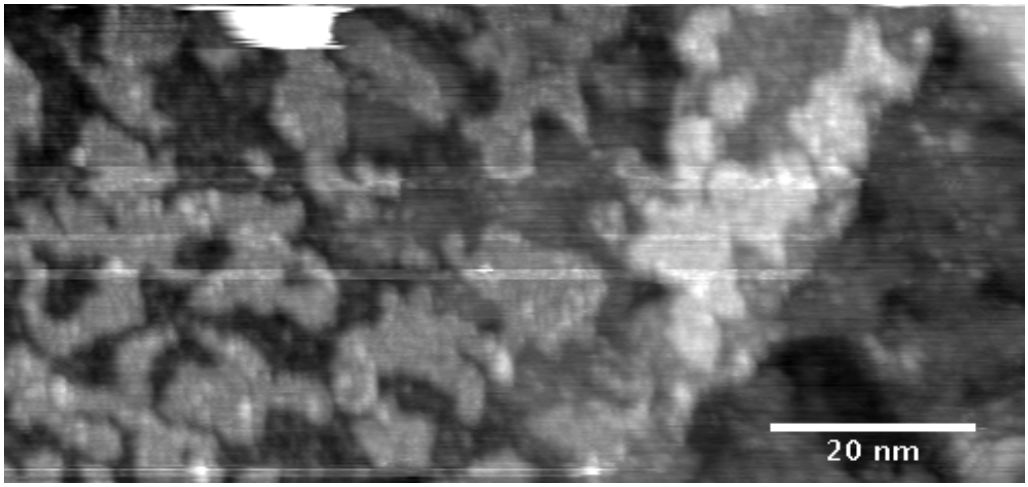

Figure 28: STM images from the same surface after annealing at 1023 K.

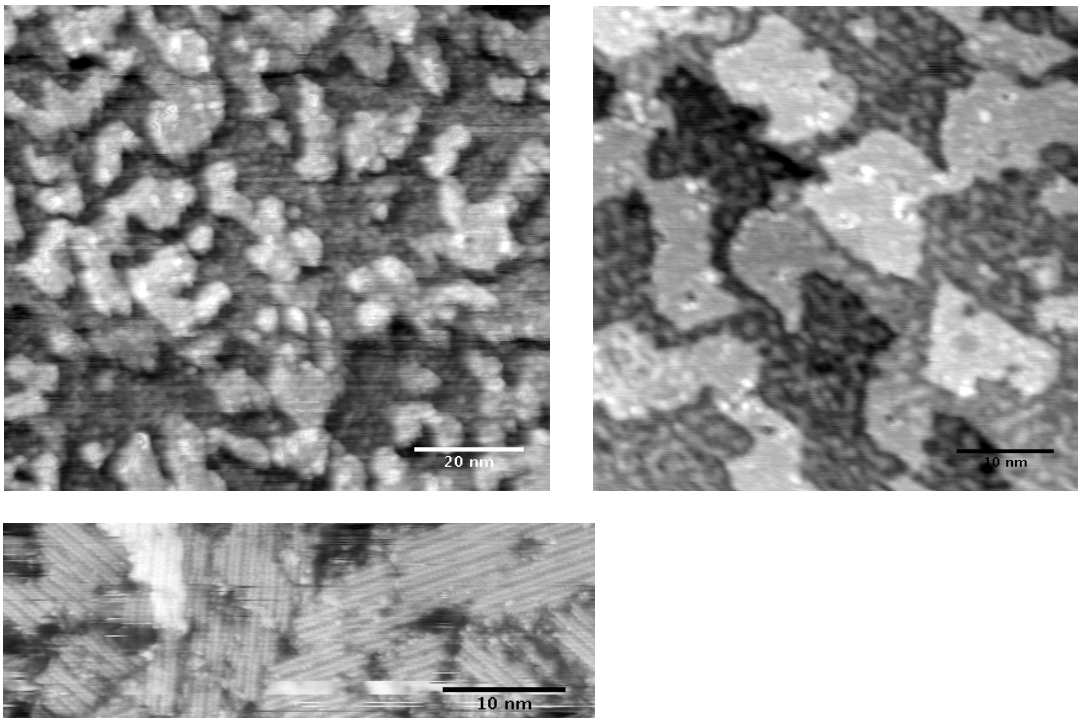

Figure 29: STM images from the same surface after annealing at 1073 K.

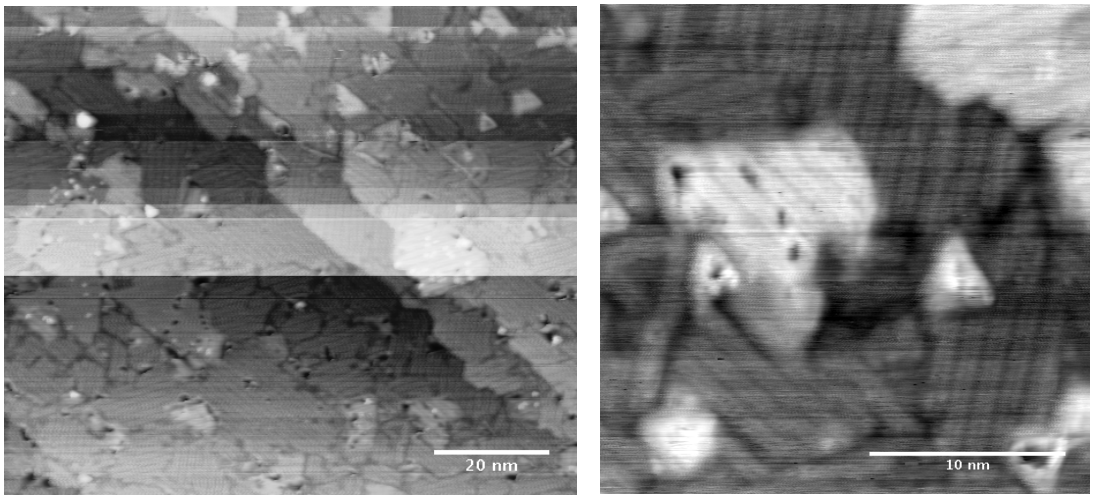

Figure 30: STM images from the same surface after annealing at 1143 K.

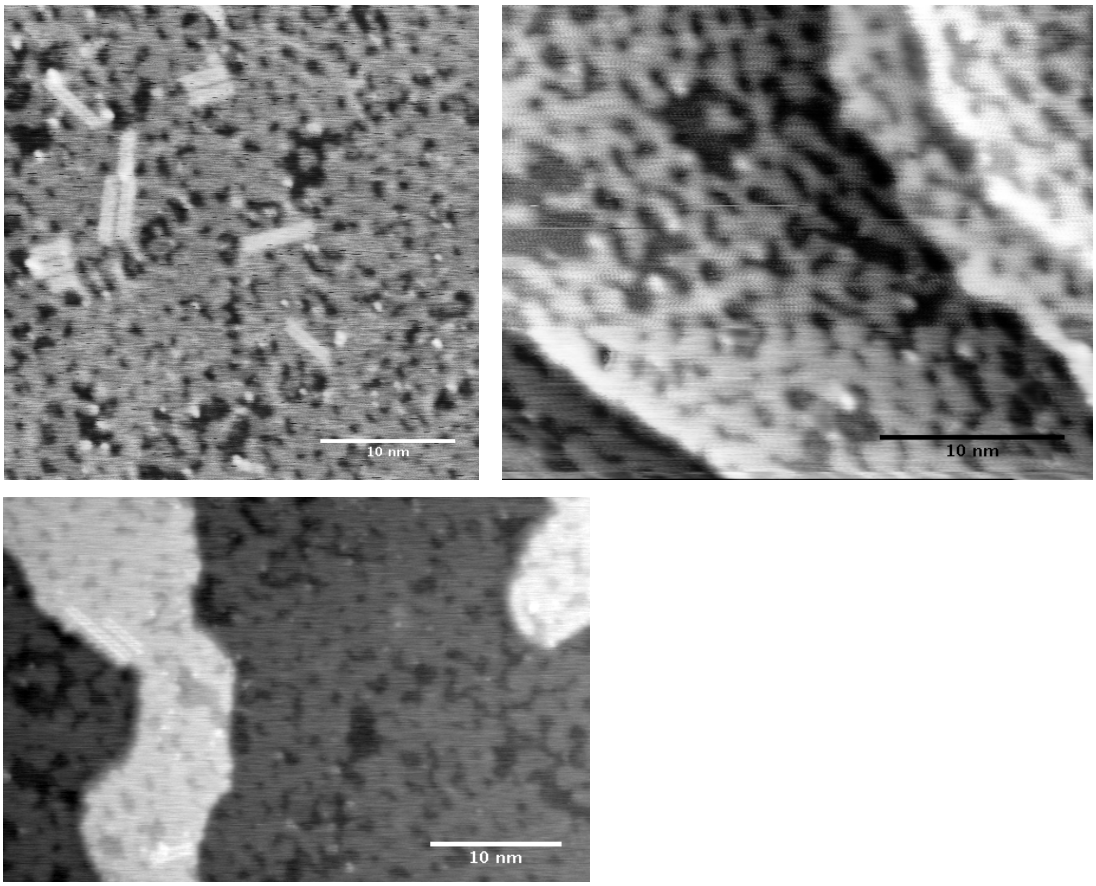

Figure 31: STM images from the same surface after annealing at 1223 K.

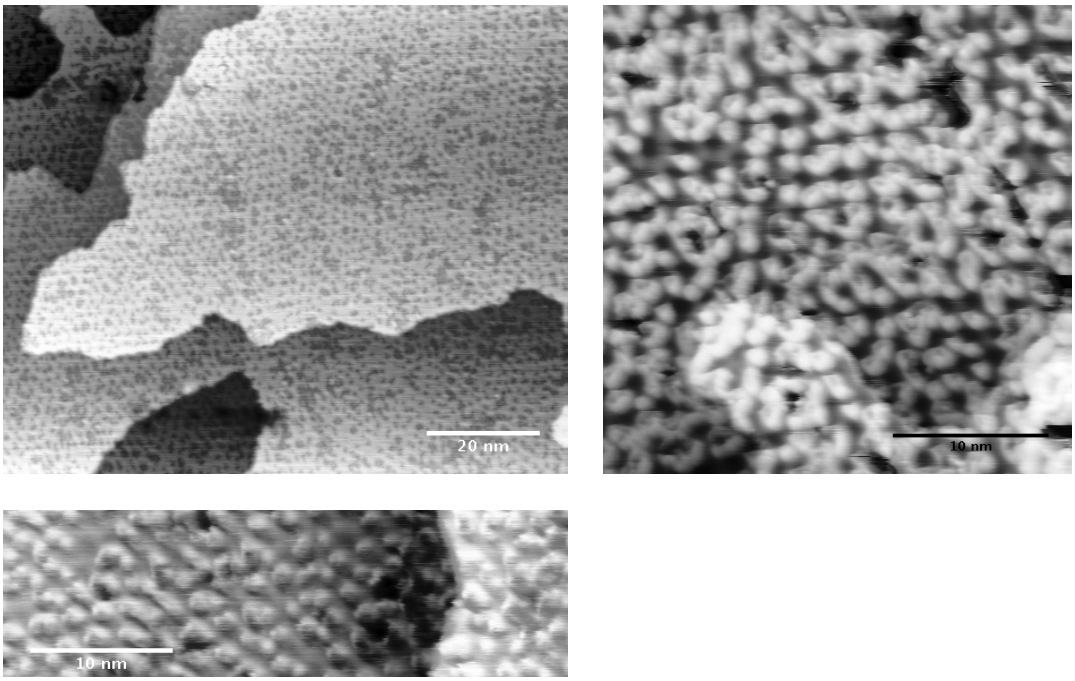

Figure 32: STM images from the same surface after annealing at 1273 K.

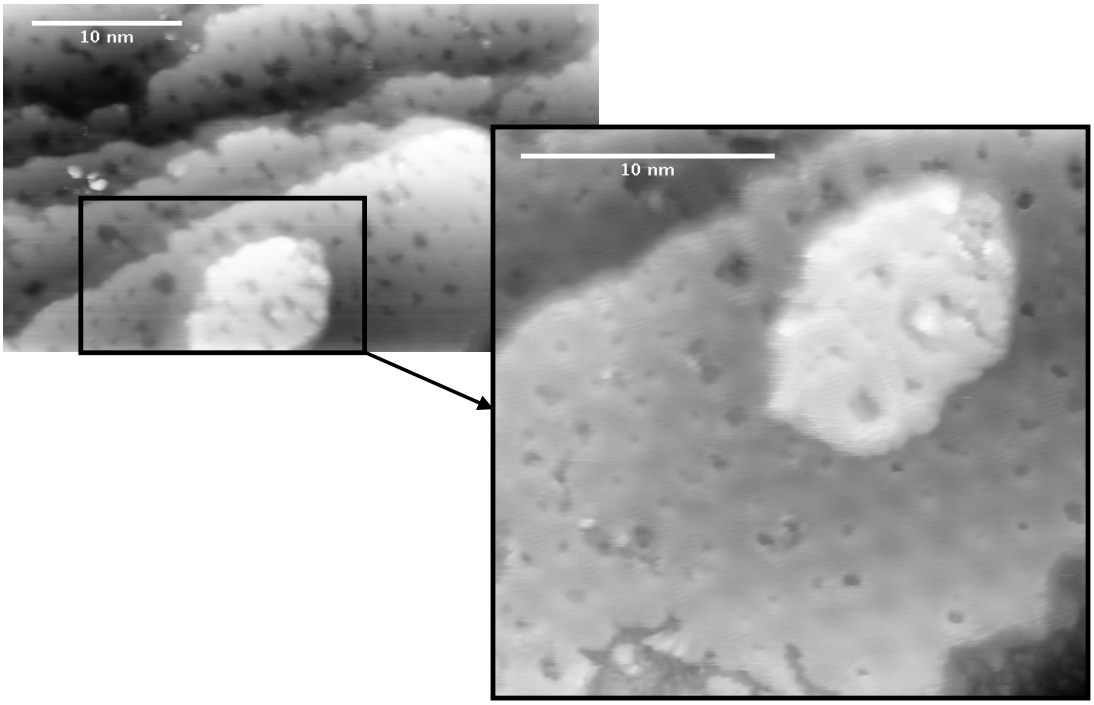

Figure 33: High resolution STM images from the same annealing step, 1273 K.